

MODELING AND SIMULATION OF SELECTIVE LASER SINTERING WITH COMSOL MULTIPHYSICS

BY SHOURYA MUKHERJEE

Senior Honors Thesis

Department of Physics and Astronomy

University of North Carolina at Chapel Hill

May 2025

Approved

Supervisor Dr. Rene Lopez

Reader Dr. Ed Samulski

Reader Dr. Louise Dolan

Abstract

This work presents a multiphysics simulation framework developed in COMSOL to model the selective laser sintering (SLS) process for both metallic (Molybdenum) and polymeric (PA12) powders. By incorporating heat transfer, fluid dynamics, phase change, and material-specific rheology, the simulations reproduce key process dynamics observed in experimental studies. The model successfully captures phenomena such as melt pool formation, open and "frozen-in" pores, bubble generation, and spatter events—exhibiting strong qualitative agreement with literature data. In particular, the PA12 simulations, which utilize a non-Newtonian viscoelastic model, reveal spatter behaviors not present in the Newtonian Molybdenum simulations, emphasizing the importance of material properties in defect formation. A comparison between 2D and 3D simulations highlights the limitations of 2D models in estimating melt efficiency, owing to unaccounted thermal losses in out-of-plane directions. These findings underscore the need for full 3D modeling to accurately predict sintering outcomes. Future work will aim to improve model fidelity through enhanced thermal modeling, stochastic powder bed configurations, and experimental validation, as well as explore data-driven optimization using machine learning.

Acknowledgements

Thank you to my supervisor Dr. Rene Lopez and his lab group for their infinite guidance and support throughout this project. Thank you to UNC Chapel Hill for access to their computational resources without which the project would have been impossible.

Declaration

I confirm that the work contained in this BSc project report has been composed solely by myself and has not been accepted in any previous application for a degree. All sources of information have been specifically acknowledged and all verbatim extracts are distinguished by quotation marks.

SignedShourya Mukherjee.....
DateFriday 9th May, 2025.....

Contents

Abstract	ii
Acknowledgements	iii
Declaration	iv
1 Introduction	1
1.1 Background	1
1.2 Literature Review	2
2 Theory	6
2.1 Melt Dynamics	6
2.2 Phase Field Method	7
2.3 Heat Transfer	8
3 Materials	11
3.1 Molybdenum	11
3.2 Polyamide 12	13
4 Methodology	17
4.1 The Complete Model	17
4.2 COMSOL Implementation	19
4.2.1 SLM 2D Implementation with Molybdenum	20
4.2.2 SLS Implementation with PA12	32
5 Results	33
5.1 Molybdenum	33
5.2 PA12	40
6 Discussion	46
6.1 Comparison with Experiment	46

6.2 Comparison between 2D and 3D Results	51
6.3 Conclusion and Future Work	52

List of Tables

3.1	Polynomial coefficients for the thermal expansion of Molybdenum using the function $\alpha(T) = a_0 + a_1T + a_2T^2 + a_3T^3$	11
4.1	Simulation parameters used for Molybdenum.	21
4.2	Material properties of Oxygen used for simulations. These expressions can be found in the COMSOL material library. For Oxygen, these expressions are valid from 150 to 600 [K].	24
4.3	Temperature-dependent viscosity function used for Molybdenum.	25
4.4	Variable definitions for the model.	26

List of Figures

3.1	Thermal expansion coefficient of Molybdenum fitted with a polynomial function $\alpha(T) = a_0 + a_1 T + a_2 T^2 + a_3 T^3$ from data obtained by Bodryakov 2014. The polynomial coefficients are listed in Table 3.1.	12
3.2	Plot of molybdenum density data from Lindemann and Blumm 2009 and Paradis, Ishikawa, and Yoda 2002	13
3.3	Thermal conductivity of PA12 as a function of temperature (J. Li et al. 2020)	14
3.4	Specific heat of PA12 as a function of temperature (J. Li et al. 2020)	15
4.1	2D geometry used for simulations with labeled parameters.	19
4.2	Particle bed geometry with labeled boundaries.	27
4.3	Particle bed geometry with labeled domains.	27
4.4	Ensure that for the phase field interface, the following domains are included in the selection for the <code>Initial Values, Fluid 2</code> node.	29
5.1	Heating profile of laser on Molybdenum with volume fraction isocontours. $D = 100 \mu\text{m}$, 20 particles total. $v_{laser} = 500 \text{ mm/s}$, $E_p = 300 \text{ W}$, and a laser penetration of $500 \mu\text{m}$	33
5.2	Temperature profile of laser on Molybdenum with volume fraction isocontours. $D = 100 \mu\text{m}$, 20 particles total. $v_{laser} = 500 \text{ mm/s}$, $E_p = 300 \text{ W}$, $r_{laser} = 50 \mu\text{m}$ and a laser penetration of $500 \mu\text{m}$	34
5.3	Heating profile of laser on Molybdenum with volume fraction isocontours. $D = 80 \mu\text{m}$, 20 particles total. $v_{laser} = 100 \text{ mm/s}$, $E_p = 150 \text{ W}$, and a laser penetration of $80 \mu\text{m}$	35
5.4	Temperature profile of laser on Molybdenum with volume fraction isocontours. $D = 80 \mu\text{m}$, 20 particles total. $v_{laser} = 100 \text{ mm/s}$, $E_p = 150 \text{ W}$, and a laser penetration of $80 \mu\text{m}$	36
5.5	Volume fraction and pressure isocontours of Molybdenum. $D = 80 \mu\text{m}$, 20 particles total. $v_{laser} = 100 \text{ mm/s}$, $E_p = 150 \text{ W}$, and a laser penetration of $80 \mu\text{m}$	36

5.6	Temperature profile of Molybdenum $D = 20 \mu m$, 20 particles total. $v_{laser} = 100 mm/s$, $E_p = 100 W$, and a laser penetration of $80 \mu m$	37
5.7	Volume fraction and pressure isocontours of Molybdenum. $D = 20 \mu m$, 20 particles total. $v_{laser} = 100 mm/s$, $E_p = 100 W$, and a laser pene- tration of $80 \mu m$	37
5.8	Process dynamics of Molybdenum. $D = 100 \mu m$, 20 particles total, and a laser penetration of $100 \mu m$ after $0.04 s$ of elapsed time.	38
5.9	Process dynamics of Molybdenum. $D = 80 \mu m$, 20 particles total, and a laser penetration of $100 \mu m$ after $0.04 s$ of elapsed time.	38
5.10	Process dynamics of Molybdenum. $D = 100 \mu m$, 20 particles total, and a laser penetration of $50 \mu m$ after $0.04 s$ of elapsed time.	39
5.11	Heating profile of PA12. $D = 100 \mu m$, 20 particles total. $v_{laser} = 500$ mm/s , $E_p = 5 W$, and a laser penetration of $500 \mu m$	40
5.12	Temperature profile of PA12. $D = 100 \mu m$, 20 particles total. $v_{laser} =$ $500 mm/s$, $E_p = 5 W$, and a laser penetration of $500 \mu m$	40
5.13	Heating profile of PA12. $D = 100 \mu m$, 20 particles total. $v_{laser} = 500$ mm/s , $E_p = 3.5 W$, and a laser penetration of $500 \mu m$	41
5.14	Temperature profile of PA12. $D = 100 \mu m$, 20 particles total. $v_{laser} =$ $500 mm/s$, $E_p = 3.5 W$, and a laser penetration of $500 \mu m$	41
5.15	Process dynamics of Polyamide. $D = 100 \mu m$, 20 particles total, and a laser penetration of $50 \mu m$ after 0.1 seconds of elapsed time.	42
5.16	Process dynamics of Polyamide. $D = 100 \mu m$, 20 particles total, and a laser penetration of $100 \mu m$ after 0.1 seconds of elapsed time.	42
5.17	Process dynamics of Polyamide. $D = 100 \mu m$, 20 particles total, and a laser penetration of $300 \mu m$ after 0.1 seconds of elapsed time.	42
5.18	A plot of the average density of the printed PA12 part when the pene- tration depth of the laser was $200 \mu m$. The density measurements were taken 0.1 seconds after the start of the simulation.	43
5.19	A plot of the average density of the printed PA12 part when the pene- tration depth of the laser was $200 \mu m$. The density measurements were taken 0.1 seconds after the start of the simulation.	44
5.20	Heating profile of PA12. $D = 100 \mu m$, 20 particles total. $v_{laser} = 100$ mm/s , $E_p = 3 W$, a laser penetration of $100 \mu m$, and an interface thickness of $\epsilon = 0.1D$	45
6.1	A figure taken from a paper by Yan et al. 2022 that showcases experimen- tal results that highlight the process dynamics of SLS with Molybdenum	46

6.2	An image taken from a paper by Leung et al. 2018 that uses X-ray in situ imaging to observe an open pore near the interface of the air and material.	47
6.3	An X-ray image cross section showing bubbles during the sintering process (Leung et al. 2018)	48
6.4	A simulation image of PA12 with an air bubble leaving the material and distorting the pressure isocontours. Highlighted is an open pore where an air bubble is accessible to the surface.	48
6.5	Highlighted image of spatter as the distortion and concentration of pressure isocontours occurs while a bubbles escapes.	49
6.6	Time evolution of isosurfaces of volume fraction in 3D simulation of polyamide with laser power of 3 W and a laser speed of 0.1 m/s. The first image on the top shows the initial configuration of the particles (there are 20 particles) and each subsequent image is 0.001 seconds apart starting from the time the laser is turned on.	50
6.7	Time evolution of 2D cross sections of volume fraction in the 3D simulation of polyamide with laser power of 3 W and a laser speed of 0.1 m/s.	51
6.8	Melting of a single particle layer with a laser power of 3 W and a laser speed of 0.1 m/s. Shown are the temperature and volume fraction at $t = 0$ s and $t = 0.03$ s. Note that the laser is turned on at $t = 0.02$ s.	52

Chapter 1

Introduction

1.1 Background

The landscape of industrial manufacturing is evolving rapidly due to the growing integration of digital technologies into production processes. This fusion of manufacturing and information systems is anticipated to drive a transformation as significant as previous industrial revolutions triggered by mechanization, mass production, and the advent of electronics. This movement is widely recognized as the Fourth Industrial Revolution, or Industry 4.0. To fully realize its potential, innovative manufacturing techniques are required to enable the swift, accurate, efficient, and adaptable creation of functional products directly from digital models.

Among the various additive manufacturing (AM) techniques, powder bed fusion methods such as Selective Laser Melting (SLM) and Selective Laser Sintering (SLS) have garnered significant attention due to their ability to fabricate complex three-dimensional structures with high precision. SLM involves the use of a high-powered laser to fully melt metallic powder, creating dense, fully functional parts, whereas SLS typically employs a lower-energy laser to sinter polymer or metal powders without fully melting them. For the purposes of this work, the term SLS will be used to refer to both of these AM techniques.

SLS offers several advantages that make it an attractive choice for advanced manufacturing applications. It provides exceptional design flexibility, allowing for the production of intricate geometries that would be difficult or impossible to achieve using traditional subtractive manufacturing techniques. Additionally, SLS supports a wide range of materials, including polymers, metals, and ceramics, making it a versatile solution for manufacturing applications within the automotive industry (Vasco 2021),

biomedical engineering (Valverde et al. 2015, Peltola et al. 2012, Evans et al. 2015), and pharmaceutical applications (Charoo et al. 2020).

Furthermore, SLS is known for its high material efficiency. Unlike conventional machining, which generates significant material waste, SLS is an additive process, meaning material usage is optimized, and excess powder can often be recycled for future builds. This efficiency contributes to cost-effectiveness and sustainability, making SLS an appealing choice for industries aiming to reduce material waste and production costs. Additionally, SLS enables the fabrication of lightweight, high-strength components by utilizing lattice structures and topology optimization, further enhancing its appeal in aerospace, automotive, and biomedical applications.

Despite these advantages, SLS faces several challenges, including limited material options compared to traditional manufacturing, inconsistent mechanical properties due to thermal gradients, and high equipment costs (Thompson et al. 2016). These challenges have motivated significant research efforts to enhance process understanding and optimization through both experimental and computational approaches (King et al. 2015).

1.2 Literature Review

Significant progress has been made in modeling selective laser sintering (SLS) and related techniques, particularly for powder bed fusion of metals. Leitz et al. employed multi-physical transient simulations in COMSOL Multiphysics to investigate the mesoscopic behavior of SLS with molybdenum powder, focusing on the effects of powder characteristics and processing parameters. Their study examined both random and grid-like arrangements of spherical particles while modeling the laser as a Gaussian heat source. The thermally coupled Navier-Stokes equations were numerically solved using a volume of fluid (VOF) approach to simulate melt dynamics (Leitz et al. 2018). While the study provided valuable qualitative insights, it did not fully account for radiative heat transfer within the powder bed.

Gu et al. 2017 explored the thermodynamic and kinetic mechanisms of selective laser melting (SLM) through multiscale computational modeling and experimental verification. Their methodology integrated mesoscale, microscale, and macroscale analyses to understand powder-laser interactions, microstructural development, and stress distribution in AlSi10Mg and Inconel 718 powders. Mesoscale modeling employed a Navier-Stokes/VOF approach, while macroscale simulations focused on temperature variations, stress evolution, and deformation across multiple layers and tracks (Gu et al. 2017).

Recent advances in metal SLS/SLM modeling have focused on multi-physics approaches

that account for complex phenomena occurring during the process. Khairallah et al. 2016 developed a high-fidelity powder-scale model that captures the physics of metal powder bed fusion processes, revealing the mechanisms behind pore formation, denudation zones, and surface roughness. Their model integrated heat transfer, fluid dynamics, and surface tension effects to provide insights into process optimization for improved part quality. Expanding on this work, Y. Yang et al. 2020 proposed a comprehensive thermo-fluid model that accounts for evaporation, recoil pressure, and Marangoni effects in metal powder bed fusion, enabling more accurate predictions of melt pool dynamics and microstructure development.

The emergence of machine learning approaches has also transformed SLS/SLM process modeling and optimization. C. Wang et al. 2021 developed a data-driven framework that combines physics-based modeling with machine learning techniques to predict defect formation in metal additive manufacturing. Their approach leverages process signatures and in-situ monitoring data to enable real-time quality control. Similarly, Baturynska, Semeniuta, and Martinsen 2018 employed artificial neural networks to optimize process parameters for improved mechanical properties and dimensional accuracy in SLS-manufactured components.

Polymers have also become widely used in additive manufacturing, but their complex structural transformations and rheology make SLS modeling more challenging. Unlike metals, polymers undergo significant phase transitions—melting, degradation, and crystallization—that introduce additional complexities in thermal and mechanical modeling. Their viscoelastic nature affects flow behavior during sintering, leading to intricate interparticle interactions and variations in densification. Effective modeling must account for these factors alongside heat transfer mechanisms such as conduction, convection, and radiation, all of which influence the final part properties.

J. Li et al. 2020 developed a thermomechanical model to simulate the sintering of Polyamide 12 (PA12) and Polyetheretherketone (PEEK), evaluating residual stress, shrinkage, and warping. Their framework incorporated thermal strain, recrystallization-induced strain, and elasto-plastic deformation while accounting for phase transformations such as melting, solidification, and recrystallization, which affect volumetric changes and stress distribution (J. Li et al. 2020). Zeng et al. approached SLS modeling for polystyrene (PS) by simulating temperature distribution and sintering mechanisms to assess the influence of laser energy density on structural warpage. Their work was validated experimentally, incorporating post-processing techniques to enhance mechanical properties (Zeng et al. 2019). However, despite these contributions, neither study accounted for fluid flow dynamics during melting, where the complex viscoelastic behavior of polymers can significantly impact printed part

quality.

Further work by J. Li et al. 2020 employed finite element simulations in COMSOL Multiphysics to model the cooling process of SLS-fabricated PA12 components. Two approximations were considered for the powder bed: one treating it as a porous solid medium and the other as a mixture of air and solid particles. Their analysis revealed that container geometry significantly influenced the cooling process, with a narrow width, extended length, and increased height yielding a more homogeneous temperature distribution and improved cooling performance (X. Li et al. 2018).

Recent developments in polymer SLS modeling have focused on multi-scale approaches that bridge molecular and continuum mechanics. Mokrane, Boutaous, and Xin 2018 developed a comprehensive numerical model for polymer powder sintering that accounts for crystallization kinetics and viscoelastic behavior. Their work demonstrated that processing parameters significantly influence crystallization rates and mechanical properties of final parts. Verbelen et al. 2016 explored the role of particle size distribution and packing density on the thermal conductivity of polymer powder beds, providing insights into optimal powder characteristics for enhanced process control.

The influence of powder characteristics on SLS/SLM outcomes has received increased attention in recent years. Sutton et al. 2017 conducted a comprehensive review of powder requirements for metal additive manufacturing, highlighting how particle morphology, size distribution, and flowability affect powder bed homogeneity and final part properties. Building on this work, Rausch et al. 2017 investigated the relationship between powder characteristics and energy absorption efficiency in polymer SLS, demonstrating that particle size and distribution significantly influence the process window and part quality.

Researchers have also focused on developing in-situ monitoring techniques to enhance process control and quality assurance in SLS/SLM. Grasso and Colosimo 2018 reviewed various sensing methodologies for metal additive manufacturing, including thermal imaging, optical tomography, and acoustic emission monitoring. These approaches enable real-time detection of defects and process anomalies, facilitating closed-loop control systems for improved reliability. Clijsters et al. 2014 demonstrated the effectiveness of melt pool monitoring for detecting lack-of-fusion defects in metal SLM, providing a foundation for quality-oriented process control.

Despite significant advances in SLS/SLM modeling and process understanding, several challenges remain. The multi-physics nature of these processes, involving complex interactions between thermal, mechanical, and fluid dynamics phenomena, requires

sophisticated computational approaches and significant computational resources. Additionally, the stochastic nature of powder bed characteristics introduces variability that is difficult to capture in deterministic models. Future research directions include the development of multi-scale, multi-physics models that integrate machine learning approaches for enhanced predictive accuracy and computational efficiency (Kamath et al. 2016).

Chapter 2

Theory

2.1 Melt Dynamics

During the liquid phase, the material flow will be modeled by the Navier-Stokes equations:

$$\frac{D\rho}{Dt} + \rho \nabla \cdot \mathbf{u} = 0 \quad (2.1)$$

$$\rho \frac{D\mathbf{u}}{Dt} = -\nabla p + \nabla \cdot \boldsymbol{\tau} + \mathbf{F} \quad (2.2)$$

where $\frac{D}{Dt} = \frac{\partial}{\partial t} + \mathbf{u} \cdot \nabla$ is the material derivative, ρ is the density, $\boldsymbol{\tau}$ is the stress tensor, and \mathbf{F} denotes external body forces. These equations are derived directly from conservation laws (Bejan 2013). The stress tensor for a Newtonian fluid is

$$\boldsymbol{\tau} = \mu \left[\nabla \mathbf{u} + (\nabla \mathbf{u})^T \right], \quad (2.3)$$

where μ is the viscosity and $\nabla \mathbf{u}$ is the gradient tensor defined as $(\nabla \mathbf{u})_{ij} = \frac{\partial u_i}{\partial x_j}$. When we assume that the fluid is incompressible, it follows that $\frac{D\rho}{Dt} = 0$, and Eqs. 2.1 and 2.2 simplify to

$$\rho \left(\frac{\partial \mathbf{u}}{\partial t} + (\mathbf{u} \cdot \nabla) \mathbf{u} \right) = -\nabla p + \mu \nabla^2 \mathbf{u} + \rho \mathbf{g} \quad (2.4)$$

$$\nabla \cdot \mathbf{u} = 0 \quad (2.5)$$

In the case of non-Newtonian flows, μ is dependent on the shear rate through some constitutive relation. For example, the Carreau model expresses the apparent viscosity μ_{app} as a function of the shear rate $\dot{\gamma}$:

$$\mu_{app}(\dot{\gamma}) = \eta_\infty + (\eta_0 - \eta_\infty) [1 + (\lambda\dot{\gamma})^2]^{\frac{n-1}{2}}, \quad (2.6)$$

where η_0 is the zero-shear viscosity, η_∞ is the infinite-shear viscosity, λ is the characteristic time constant, n is the power-law index that determines the degree of shear thinning, and $\dot{\gamma}$ is the shear rate.

Here, the Navier Stokes equations become:

$$\rho \left(\frac{\partial \mathbf{u}}{\partial t} + (\mathbf{u} \cdot \nabla) \mathbf{u} \right) = -\nabla p + \mu_{app} \nabla^2 \mathbf{u} + \rho \mathbf{g} \quad (2.7)$$

$$\nabla \cdot \mathbf{u} = 0 \quad (2.8)$$

2.2 Phase Field Method

We use the phase field formulation to model the multiphase flow of air and the material. The phase field uses a phase variable ϕ to track the air and material domains, where $-1 \leq \phi \leq 1$. The volume fraction is defined as:

$$V_1 = \frac{1 - \phi}{2}, \quad V_2 = \frac{1 + \phi}{2} \quad (2.9)$$

The time evolution of ϕ follows the Cahn-Hilliard equation:

$$\frac{\partial \phi}{\partial t} + \mathbf{u} \cdot \nabla \phi = \nabla \cdot (M \nabla G) \quad (2.10)$$

$$G = \frac{\lambda}{\epsilon^2} (-\epsilon^2 \nabla \phi + (\phi^2 - 1)\phi) \quad (2.11)$$

where G is a help variable that is related to the chemical potential, M is a parameter controlling the diffusion time scale, and ϵ is the interface width Yue 2020.

The coupled momentum equation is:

$$\rho \left(\frac{\partial \mathbf{u}}{\partial t} + (\mathbf{u} \cdot \nabla) \mathbf{u} \right) + \mathbf{J} \cdot \nabla \mathbf{u} = -\nabla p + \mu \nabla^2 \mathbf{u} + G \nabla \phi + \rho \mathbf{g}, \quad (2.12)$$

where volume-averaged density and viscosity are given by:

$$\rho = \rho_{air} V_1 + \rho_{mat} V_2, \quad \mu = \mu_{air} V_1 + \mu_{mat} V_2 \quad (2.13)$$

From the phase field method, the surface tension can be modelled as:

$$\mathbf{F}_{st} = \frac{\lambda}{\epsilon^2} G \nabla \phi \quad (2.14)$$

where the phase parameters λ and χ relate to surface tension σ as:

$$\lambda = \frac{3\epsilon\sigma}{\sqrt{8}}, \quad \chi = \frac{9M\sigma^2}{8\lambda^2} \quad (2.15)$$

2.3 Heat Transfer

The heat transfer equation is given by:

$$\rho C_p \left(\frac{\partial T}{\partial t} + \mathbf{u} \cdot \nabla T \right) + \nabla \cdot (k \nabla T) = Q \quad (2.16)$$

where T is temperature, C_p is the specific heat at constant pressure, k is the thermal conductivity, and Q is a volumetric heat source.

We can incorporate a viscosity-temperature to the Navier Stokes through:

$$\mu_{mat} = \mu_{mat}(T) \quad (2.17)$$

We can also incorporate a similar coupling with the specific heat capacity.

$$C_{p,mat} = C_{p,mat}(T) \quad (2.18)$$

The volume-averaged properties are:

$$k = k_{air} V_1 + k_{mat} V_2, \quad C_p = C_{p,air} V_1 + C_{p,mat} V_2 \quad (2.19)$$

The heat source Q includes laser heating Q_{laser} and radiative heat transfer contributions Q_r . Previous modeling efforts (J. Li et al. 2020, Leitz et al. 2018) have used a Gaussian laser heating distribution with a Beer-Lambert attenuation term, which manifests itself as:

$$Q_{laser} = A \frac{E_p}{\pi D r_{laser}^2} \exp \left(-\frac{(x - x_r)^2 + (y - y_r)^2}{r_{laser}^2} \right) \exp(-\beta_{laser} z) \quad (2.20)$$

where A is an absorption constant, E_p is the laser power, r_{laser} is the laser radius, D is the particle size, and β_{laser} is the extinction coefficient of the laser.

We will say that $\beta_{laser} = 1/d_{laser}$, where d_{laser} is the penetration depth of the laser. This is the distance it takes for the laser's intensity to diminish by about 2/3.

In order to fully model radiative heat transfer with scattering, it is necessary to solve the radiative transfer equation:

$$\hat{\mathbf{s}} \cdot \nabla I(s) = \kappa I_b - \beta I(s) + \frac{\sigma_s}{4\pi} \int_{4\pi} I(\Omega) \phi(\Omega, s) d\Omega \quad (2.21)$$

$$I_b = \frac{n_r^2 \sigma_s T^4}{\pi} \quad (2.22)$$

where $I(s)$ is intensity in the \mathbf{s} direction of emission, κ is the absorption coefficient, β is the extinction coefficient, σ_s is the Stefan-Boltzmann constant, n_r is the index of refraction of the surrounding medium, $d\Omega$ is a steradian differential, and $\phi(\Omega, s)$ is a scattering phase function.

For linearly anisotropic media, it is $\phi(\Omega, s) = 1 + a_1 \mu_0$, where μ_0 is the permeability of free space.

For optically thick mediums, we can approximate the heat exchanges of Equation 2.21 using the P_1 approximation, which leads to a Poisson-type equation:

$$-\nabla \cdot (D_{P_1} \nabla G) = -Q_r \quad (2.23)$$

$$D_{P_1} = \frac{1}{3\kappa + \sigma_{scatter}(3 - a_1)} \quad (2.24)$$

where $Q_r = \kappa(G - 4\pi I_b)$, with boundary conditions:

$$-\mathbf{n} \cdot (D_{P_1} \nabla G) = -q_{r,net} \quad (2.25)$$

$$q_{r,net} = \frac{\epsilon}{2(2-\epsilon)} (4\pi I_b - G) \quad (2.26)$$

where ϵ is the emissivity of the wall (Modest and Mazumder 2021).

Chapter 3

Materials

3.1 Molybdenum

The melting point of Molybdenum is known to be $T_m = 2896[K]$ and the heat of fusion is $H_f = 33.6[kg \cdot mol^{-1}]$. Paradis, Ishikawa, and Yoda [2002](#) measured the density and specific heat of molybdenum using an electrostatic levitation furnace developed by NASDA. The furnace levitated the sample in a vacuum chamber, heated by laser beams, and controlled its position with feedback loops. Through this methodology, the specific heat capacity of liquid molybdenum was found to be $C_{pL} = 34.2 + 1.13 \times 10^{-3}(T - T_m)[J \cdot mol^{-1} \cdot K^{-1}]$ (Paradis, Ishikawa, and Yoda [2002](#)).

A similar method was also used by Paradis, Ishikawa, and Koike [2007](#) to find the surface tension and viscosity of Molybdenum. The surface tension was found to be $\sigma(T) = 2.29 \times 10^3 - 0.26(T - T_m)[mN \cdot m^{-1}]$ and the viscosity was fitted to an Arrhenius equation as $\mu(T) = 0.27 \exp[73 \times 10^3 / (RT)][mPa \cdot s]$, where R is the universal gas constant (Paradis, Ishikawa, and Koike [2007](#)).

Coefficient	Value
a_0	12.270764915751679
a_1	0.008718337229355673
a_2	$-7.799703040318278 \times 10^{-6}$
a_3	$5.77704867949318 \times 10^{-9}$

Table 3.1: Polynomial coefficients for the thermal expansion of Molybdenum using the function $\alpha(T) = a_0 + a_1T + a_2T^2 + a_3T^3$.

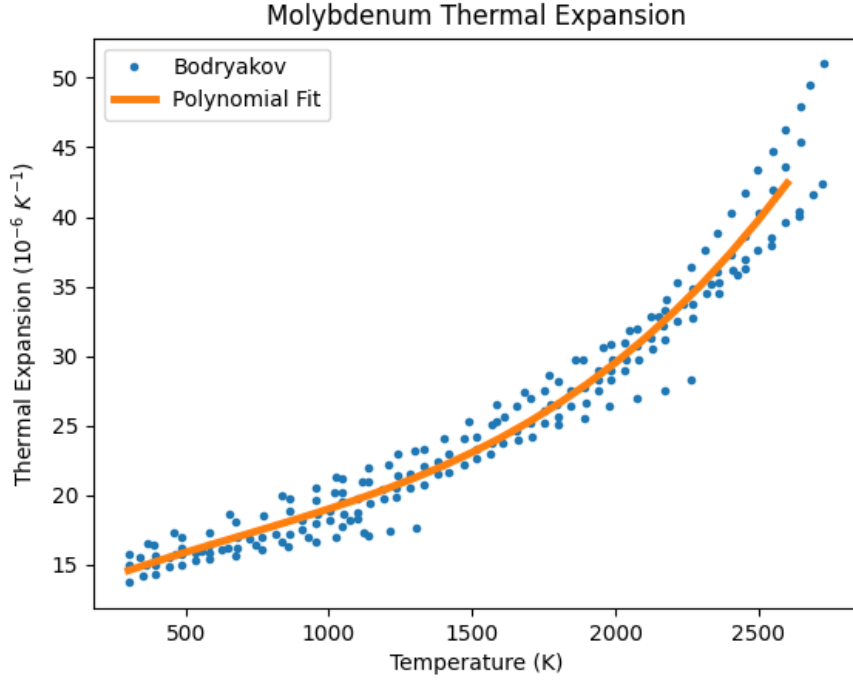


Figure 3.1: Thermal expansion coefficient of Molybdenum fitted with a polynomial function $\alpha(T) = a_0 + a_1T + a_2T^2 + a_3T^3$ from data obtained by Bodryakov 2014. The polynomial coefficients are listed in Table 3.1.

The thermal expansion coefficient of Molybdenum was measured as a function of temperature by Bodryakov 2014 up to the melting point. A polynomial fit of the data is shown in Figure 3.1. By definition, the thermal expansion is related to the density by:

$$\frac{d\rho}{dT} = -\rho\alpha \quad (3.1)$$

Since $\alpha = \alpha(T)$ is dependent on temperature, then the solution to the differential equation:

$$\frac{d\rho(T)}{dT} = -\rho(T)\alpha(T) \quad (3.2)$$

can be written as $\rho(T) = \rho_0 \exp(-\int_{T_0}^T \alpha(T')dT')$ for the initial condition $\rho(T_0) = \rho_0$. In the case of a polynomial fit, $\alpha(T) = a_0 + a_1T + a_2T^2 + a_3T^3$ then

$$\rho(T) = \rho_0 \exp \left(a_0(T_0 - T) + \frac{a_1}{2}(T_0^2 - T^2) + \dots + \frac{a_3}{4}(T_0^4 - T^4) \right) \quad (3.3)$$

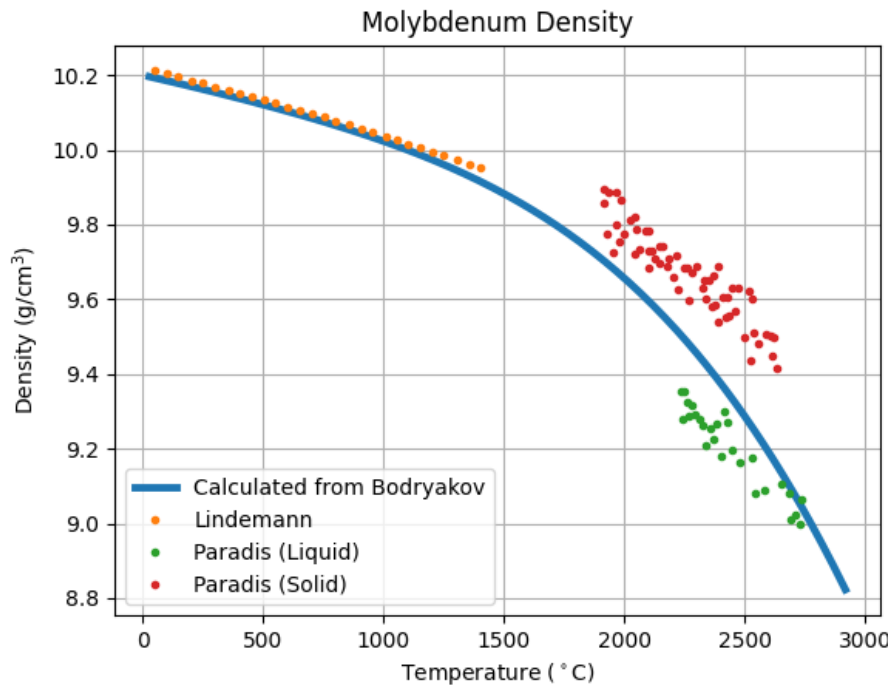


Figure 3.2: Plot of molybdenum density data from Lindemann and Blumm 2009 and Paradis, Ishikawa, and Yoda 2002

The density of Molybdenum is known to be 10.2 g/cm^3 at room temperature (Lindemann and Blumm 2009). So we can use this initial condition to obtain a fit of density, which is shown in Figure 3.2 along with data collected by Lindemann and Blumm 2009 and Paradis, Ishikawa, and Yoda 2002.

The emissivity of Molybdenum has been shown to depend on surface roughness and temperature. He et al. 2024 found by measuring emissivity for molybdenum with roughness ranging from 5 to 103 nm at temperatures of 25, 600, 800, and 1030°C that both for molybdenum with a flat surface, emissivity remains low (below 0.1) at temperatures between 600–1000°C. However, samples with higher surface roughness exhibit higher emissivity, which varies significantly with temperature.

3.2 Polyamide 12

Polyamide 12 (PA12) is a semi-crystalline engineering thermoplastic renowned for its low water absorption, high impact strength, and excellent chemical resistance Robert

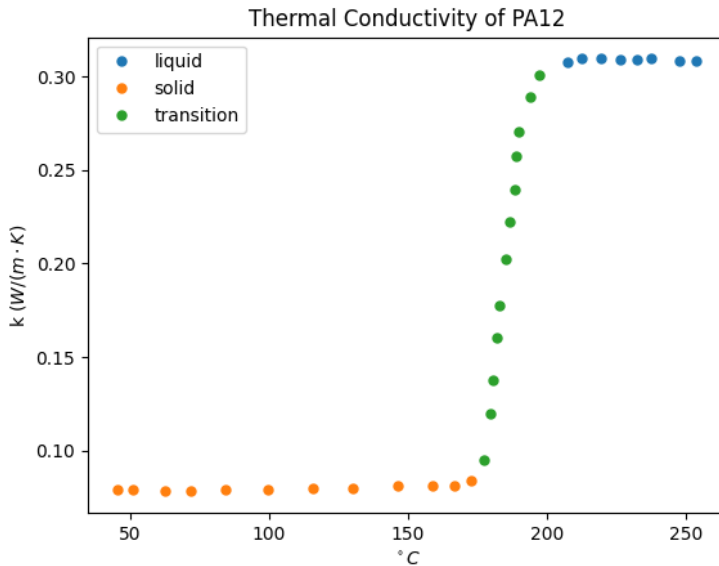


Figure 3.3: Thermal conductivity of PA12 as a function of temperature (J. Li et al. 2020)

et al. 2004. The material has a melting temperature between 170°C and 180°C, a decomposition temperature ranging from 465°C to 475°C, and a glass transition temperature around 40°C to 50°C. PA12 possesses a Young's modulus of 1400 MPa, a density between 1.01 and 1.04 g/cm³, and a thermal conductivity of 0.22 to 0.24 W/(m·K). Differential scanning calorimetry (DSC) measurements have been used to reveal its thermal transitions and have shown an enthalpy of melting to be approximately 34 J/g.

Peyre et al. 2015 conducted an analysis on the selective laser sintering (SLS) of two semi-crystalline polymers, PA12 and PEKK, using a dual experimental-numerical approach. They developed a specialized SLS setup with comprehensive diagnostics, including thermal cameras and pyrometers, to investigate laser-powder interaction mechanisms. Their study found that laser transmission through polymer powder beds follows a Beer-Lambert attenuation law, with extinction coefficients of approximately 7500 m⁻¹ for both materials, and only about 40% of the incident laser energy contributes to the polymer melting process (Peyre et al. 2015).

The temperature dependent thermal conductivity and specific heat capacity are obtained from experimental data collected by J. Li et al. 2020. The thermal conductivity and specific heat of PA12 are plotted in Figures 3.3 and 3.4 respectively.

The temperature dependence of the viscosity of PA12 is described using the temperature

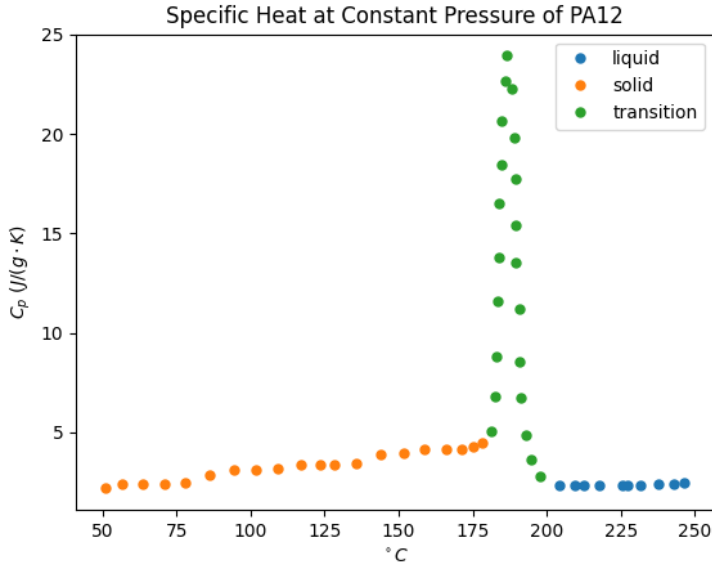


Figure 3.4: Specific heat of PA12 as a function of temperature (J. Li et al. 2020)

shift factor a_T based on the Arrhenius equation. The Arrhenius approach is particularly suitable for describing the temperature dependence of viscosity in semi-crystalline thermoplastics like PA12. The temperature shift factor a_T is given by:

$$a_T(T) = \exp\left(\frac{E_0}{R}\left(\frac{1}{T} - \frac{1}{T_0}\right)\right)$$

where E_0 is the material-dependent flow activation energy, R is the ideal gas constant, T is the temperature, and T_0 is the reference temperature (Johannes Wortberg et al. 2012).

This shift factor allows the viscosity to be adjusted for different temperatures as a_T is integrated into the Carreau model to account for the temperature dependence of viscosity. The modified Carreau model expresses the apparent viscosity as

$$\mu_{app}(\dot{\gamma}, T) = \frac{A \cdot a_T(T)}{\left[1 + (B \cdot a_T(T) \cdot \dot{\gamma})^2\right]^C}$$

where A is the zero shear viscosity (η_0), which is temperature-dependent through a_T , B is the transition time, also scaled by a_T , C is the viscosity exponent, which remains constant, $\dot{\gamma}$ is the shear rate, and $a_T(T)$ is the temperature shift factor by Arrhenius, which adjusts the viscosity based on the temperature. The key effects are as follows:

a_T scales the zero shear viscosity A , reducing it at higher temperatures, reflecting the material's easier flow at elevated temperatures. The transition time B , marking the shift from Newtonian to shear-thinning behavior, is also scaled by a_T , indicating faster transitions at higher temperatures. The model predicts lower viscosities at higher temperatures due to the influence of a_T , aligning with the physical behavior of PA12 during processes like laser sintering. This integration ensures that the Carreau model accurately represents the combined effects of shear rate and temperature on the viscosity of PA12 (Mielicki, Gronhoff, and Wortberg 2014).

The viscosity of PA12 also varies significantly with aging time due to structural changes in the material. This variation is described using the structural change shift factor a_{SC} , which accounts for the combined effects of time and temperature on the viscosity. As PA12 ages, its viscosity increases due to molar mass build-up, understood as post-condensation. This structural change results in longer molecular chains, which restrict molecular movement and increase viscosity. The viscosity increase follows an exponential growth behavior, approaching an upper limit over time (Mielicki, Gronhoff, and Wortberg 2014, Johannes Wortberg et al. 2012).

The shift factor a_{SC} is used to describe the time and temperature dependence of viscosity due to structural changes. It is expressed as:

$$a_{SC}(t, T) = a_{SC,UL} - (a_{SC,UL} - 1) \cdot \exp\left(-k_0 \cdot t \cdot \exp\left(-\frac{E_{0,SC}}{R \cdot T}\right)\right)$$

where $a_{SC,UL}$ is the upper limit of structural change, k_0 is the rate of structural change, $E_{0,SC}$ is the structural change activation energy, R is the ideal gas constant, t is the aging time, and T is the temperature. The viscosity increases significantly during the initial aging period (up to about 20 hours), reflecting rapid structural changes. After this initial period, the rate of viscosity increase slows down, approaching an upper limit as the material continues to age. Higher temperatures can accelerate the structural changes, leading to faster increases in viscosity.

Thus, the complete viscoelastic model for PA12 can be expressed as:

$$\eta(\dot{\gamma}, T) = \frac{A \cdot a_T(T) a_{SC}(t, T)}{\left[1 + (B \cdot a_T(T) \cdot a_{SC}(t, T) \cdot \dot{\gamma})^2\right]^C}.$$

Chapter 4

Methodology

4.1 The Complete Model

For Molybdenum, we model the fluid phase as Newtonian and incompressible, in order to avoid additional model complexity. Past work by Leitz et al. 2018 also utilizes these assumptions, but unlike this previous work, our current work invokes the P1 approximation to simulate radiative heating in a thermodynamically accurate way.

We also make the additional assumptions that the laser is only heating the material phase and that only the material is radiating thermal energy. Thus, the air phase has no emissivity in this current model. Finally, we assume the scattering coefficient $\sigma_s = 0$ and that $a_1 = 0$, indicating isotropic scattering. These assumptions do not have much consequence under the P_1 approximation other than a slight change to the diffusion parameter D_{P_1} . With these approximations, the model equations for SLS consist of the fluid dynamics equations:

$$\rho \left(\frac{\partial \mathbf{u}}{\partial t} + (\mathbf{u} \cdot \nabla) \mathbf{u} \right) = -\nabla p + \mu \nabla^2 \mathbf{u} + \rho \mathbf{g} + \mathbf{F}_{st} \quad (4.1)$$

$$\nabla \cdot \mathbf{u} = 0 \quad (4.2)$$

the phase field equations:

$$\frac{\partial \phi}{\partial t} + \mathbf{u} \cdot \nabla \phi = \nabla \cdot (M \nabla G) \quad (4.3)$$

$$G = \frac{\lambda}{\epsilon^2}(-\epsilon^2 \nabla \phi + (\phi^2 - 1)\phi) \quad (4.4)$$

the heat transfer equation:

$$\rho C_p \left(\frac{\partial T}{\partial t} + \mathbf{u} \cdot \nabla T \right) + \nabla \cdot (k \nabla T) = Q_{laser} + Q_r \quad (4.5)$$

the laser heating equation:

$$Q_{laser} = A_{mat} V_2 \frac{E_p}{\pi D r_{laser}^2} \exp \left(-\frac{(x - x_r)^2 + (y - y_r)^2}{r_{laser}^2} \right) \exp(-\beta_{laser} z) \quad (4.6)$$

and, the radiation heat transfer equations assuming no scattering:

$$-\nabla \cdot (D_{P_1} \nabla G) = -Q_r \quad (4.7)$$

$$D_{P_1} = \frac{1}{3\kappa} \quad (4.8)$$

In addition, we have the following multiphysics couplings:

$$\rho = \rho_{air} V_1 + \rho_{mat} V_2, \quad \mu = \mu_{air} V_1 + \mu_{mat} V_2 \quad (4.9)$$

$$k = k_{air} V_1 + k_{mat} V_2, \quad C_p = C_{p,air} V_1 + C_{p,mat} V_2 \quad (4.10)$$

$$\mathbf{F}_{st} = \frac{\lambda}{\epsilon^2} G \nabla \phi \quad (4.11)$$

We are also free to include temperature dependencies in the viscosity and specific heat capacity to account for phase transition during the sintering:

$$C_{p,mat} = C_{p,mat}(T), \quad \mu_{mat} = \mu_{mat}(T) \quad (4.12)$$

In the case of PA12, we must also account for the viscoelastic relation of Equation 4.1. We couple the rheological model to the existing physics in the following way:

$$\mu = \mu_{air}V_1 + \mu_{app}V_2 \quad (4.13)$$

where μ_{app} is given by the equation,

$$\mu_{app}(\dot{\gamma}, T) = \frac{A \cdot a_T(T)}{\left[1 + (B \cdot a_T(T) \cdot \dot{\gamma})^2\right]^C}$$

and the shear rate is calculated from the velocity field \mathbf{u} as

$$\dot{\gamma} = \sqrt{2\mathbf{S} : \mathbf{S}} \quad (4.14)$$

where $\mathbf{S} : \mathbf{S} = \text{tr}(\mathbf{S}^T \mathbf{S})$ is the Frobenius product of the two matrices and \mathbf{S} is the strain tensor defined as

$$\mathbf{S} = \frac{1}{2}(\nabla \mathbf{u} + (\nabla \mathbf{u})^T). \quad (4.15)$$

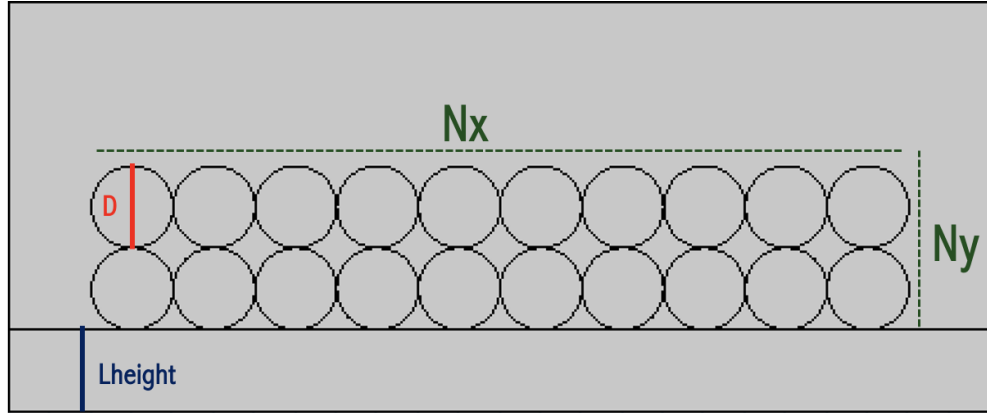


Figure 4.1: 2D geometry used for simulations with labeled parameters.

4.2 COMSOL Implementation

We use the finite element software COMSOL Multiphysics to solve the model with Molybdenum and PA12. The following procedure was done in COMSOL 6.1. The Java codes for these simulations can also be found at the Github repository at <https://github.com/finalbossqc/SLS>.

4.2.1 SLM 2D Implementation with Molybdenum

Create a New Model

1. Open COMSOL Multiphysics.
2. Go to `File → New` to create a new model.
3. Create a blank simulation.
4. Add a 2D component.

Define Parameters

1. Navigate to `Global Definitions → Parameters 1`.
2. Add the following parameters with appropriate names, values, and descriptions (optional) as shown in Figure 4.1.

Symbol	Value	Description
R	8.31446261815324 [J/(mol*K)]	Gas constant
T0	50 [degC]	Initial temperature
Tamb	T0	Ambient temperature
dwidth	100 [um]	Boundary thickness
epsilon	0.15*D	Interface thickness
D	100 [um]	Particle size
Nx	10	Particles in x-direction
<td>2</td> <td>Particles in y-direction</td>	2	Particles in y-direction
Lheight	100 [um]	Layer height
vlaser	500 [mm/s]	Laser speed
Ep	300 [W]	Laser power
laserpenetration	500 [um]	Penetration depth
A	0.5	Absorption factor
rlaser	50 [um]	Laser radius
xr	onlocation - vlaser * ontime	
yr	Lheight + D*Ny	
onlocation	2*D + D/2	
ontime	0.02 [s]	
offtime	0.16 [s]	
Dp1	1/(3*kappa)	Radiation factor
n	1	
kappa	1/pd	Absorption coefficient
sigma_b	5.67e-8 [W/(m^2*K^4)]	Stefan-Boltzmann constant
pd	80 [um]	Light penetration depth

Table 4.1: Simulation parameters used for Molybdenum.

Set Up Geometry

1. Navigate to Component 1 → Geometry 1.
2. Right-click Geometry 1 and add Circle
3. Navigate to Geometry 1 → Circle 1
4. Set Radius to D/2
5. Set Sector Angle to 360
6. Navigate to Base and from the drop down menu, select Center

7. Set the **x** and **y** positions to $1.5*D$ and $0.5*D + Lheight$
8. Right-click **Geometry 1** and add **Array**.
9. Navigate to **Geometry 1 → Array 1**.
10. For **Array Type** select **Rectangular**
11. For **x size** and **y size**, enter **Nx** and
12. For **Displacement** in the **x** and **y** directions, enter **D** and **D** for both fields.
13. For **Input objects** choose the tag of the previously created Circle object **c1**.
14. Right-click **Geometry 1** and add two **Rectangle** objects.
15. Navigate to **Geometry 1 → Rectangle 1**.
16. Set the **Base** to **Corner**.
17. Set the **Width** to $D*(Nx+2)$.
18. Set the **Height** to $Lheight + D*Ny*2$
19. Navigate to **Geometry 1 → Rectangle 2**.
20. Set the **Base** to **Corner**.
21. Set the **Width** to $D*(Nx+2)$.
22. Set the **Height** to **Lheight**

Define Functions

1. Right-click **Definitions → Functions → Rectangle**.
2. Set the **Function name** to **onoff**.
3. Set the **Lower limit** to **ontime**
4. Set the **Upper limit** to **offtime**
5. Set the **Baseline** to **0**
6. Set the **Amplitude** to **1**
7. For smoothing, set the **Size of the transition zone** to **0.001**.
8. Set the **Number of continuous derivatives** to **2**.
9. Right-click **Definitions → Functions → Gaussian Pulse**.

10. Set the **Function name** to `delta`.
11. Set the **Location** to 0.
12. Set the **Standard deviation** to 5.
13. Set the **Baseline** to 0.
14. Set the **Normalization** to **Integral**.
15. Set the **Integral** value to 1.

Material Definitions

1. We will only mention that material properties that are relevant to the physics interfaces.
2. Right-click on **Materials** under **Component 1**, and select **Add Material**.
3. In the **Materials** settings, click on the **Material Browser** (located next to the **Material Name** field).
4. Search for **Oxygen** (you can use predefined materials from COMSOL or define a custom one)
5. Set the **Name** of the material to `mat1`.
6. Ensure that the following material properties are defined for the **Oxygen** material. They should be available through the COMSOL material library, but if they aren't, these are the full expressions of the material properties as functions of temperature.

	Function	Function expression	Units
μ_{air}	<code>mat1.def.eta(T [K])</code>	-5.55818182E-7+9.24202797E-8*T^1- 8.71841492E-11*T^2+4.82983683E- 14*T^3	Pa*s
$C_{p,air}$	<code>mat1.def.Cp(T [K])</code>	959.514545- 0.416383077*T^1+7.63158508E- 4*T^2+1.46018648E-6*T^3- 3.24009324E-9*T^4+1.6E-12*T^5	J/(g*K)
ρ_{air}	<code>mat1.def.rho(1 atm, T)</code>	pA*0.032/R_const/T	kg/m^3
k_{air}	<code>mat1.def.k(T [K])</code>	-0.0070110303+1.688723E-4*T^1- 2.28911422E-7*T^2+1.6991453E-10*T^3	W/(m*K)

Table 4.2: Material properties of Oxygen used for simulations. These expressions can be found in the COMSOL material library. For Oxygen, these expressions are valid from 150 to 600 [K].

7. Right-click on **Materials** again, and select **Add Blank Material** to create a new material for **Molybdenum**.
8. Set the **Name** to **mat2**
9. Ensure that the following material properties are included.

	Function	Function expression	Units
$C_{p,mat}$	<code>mat2.def.Cp(T [K])</code>	(34.2 + 1.13E-3 * (T-2896[K])) * (1/95.5) + 3.5183E5 * delta(T-2896[K])	J/(g*K)
σ	<code>mat2.def.sigma(T [K])</code>	(2.29E3 - 0.26 * (T - 2896 [K])) * 0.001	N/m
ρ_{mat}	<code>mat2.def.rho(T [K])</code>	10.2*exp(12.270764915751679E-6*(273 - T) + 0.008718337229355673E-6*(273^2 - T^2)/2 - 7.799703040318278E-12*(273^3 - T^3)/3 + 5.77704867949318E-15*(273^4 - T^4)/4)	g/cm^3
k_{mat}	<code>mat2.def.k(T [K])</code>	138	W/(m*K)

10. For the viscosity, right-click on **Materials** → **Molybdenum** → **Basic** and go to **Functions** → **Piecewise**.
11. Set the function name to μ . Set the size of the transition zone to 0.1 and set the piecewise function to match Table 4.3. Notice that we set the viscosity to be

constant in parts of the temperature range. This is done to reduce numerical artifacts that occur during the cooling process.

T_{min} [K]	T_{max} [K]	Viscosity Function [Pa·s]
200	500	120
500	3000	$0.27 \cdot \exp(73000/(R \cdot T)) \cdot 0.001$

Table 4.3: Temperature-dependent viscosity function used for Molybdenum.

12. **Alternative:** Download the Github at <https://github.com/finalbossqc/SLS>. In the directory `SLS > Materials`, there is an XML file containing the materials used for these simulations. Right-click on `Materials` and select `Import Materials` and select the XML file in the file browser. This will load the materials into the COMSOL model.

Variable Definitions

1. Click on `Component 1`
2. Right click on `Definition 1` and add `Variables` if not already added.
3. Add the following variables from Table 4.4.

Symbol	Value	Description
Ed	$E_p / (D \pi r_{laser}^2)$	Laser energy density (W/m^3)
Gspace	$\exp(-(x - (x_r + v_l t))^2 / (2 r_{laser}^2))$	Gaussian spatial distribution of laser energy
BeerLambert	$\exp((y - y_r) / \text{laserpenetration})$	Beer-Lambert absorption factor in y-direction
Qlaser	$A * Ed * Gspace * \text{onoff}(t) * BeerLambert * pf.Vf2$	Volumetric laser heat source (W/m^3)
k	$\text{mat1.def.k}(T_0) * pf.Vf1 + \text{mat2.def.k}(T) * pf.Vf2$	Thermal conductivity ($\text{W}/(\text{m}\cdot\text{K})$)
rho	$\text{mat1.def.rho}(1 \text{ atm}, T_0) * pf.Vf1 + \text{mat2.def.rho}(T_0) * pf.Vf2$	Density (kg/m^3)
Cp	$\text{mat1.def.Cp}(T_0) * pf.Vf1 + \text{mat2.def.Cp}(T) * pf.Vf2$	Heat capacity at constant pressure ($\text{J}/(\text{kg}\cdot\text{K})$)
mu	$\text{mat1.def.eta}(T_0) * pf.Vf1 + \text{mat2.def.mu}(T) * pf.Vf2 + 0.005$	Dynamic viscosity ($\text{Pa}\cdot\text{s}$)
sigma	$\text{mat2.def.sigma}(T)$	Surface tension (N/m)
lambda	$3 \epsilon * \sigma / \sqrt{8}$	Capillary pressure coefficient (N)
Fstx	$\lambda / \epsilon^2 * \psi * \phi_{ipfx}$	Surface tension force in x-direction (N/m^3)
Fsty	$\lambda / \epsilon^2 * \psi * \phi_{ipfy}$	Surface tension force in y-direction (N/m^3)
Qr	$\kappa * (\text{Grad} - 4 \pi * I_b)$	Radiative heat loss (W/m^3)
Ib	$n^2 * \sigma_b * T^4 / \pi * pf.Vf2$	Blackbody radiation intensity (W/m^2)

Table 4.4: Variable definitions for the model.

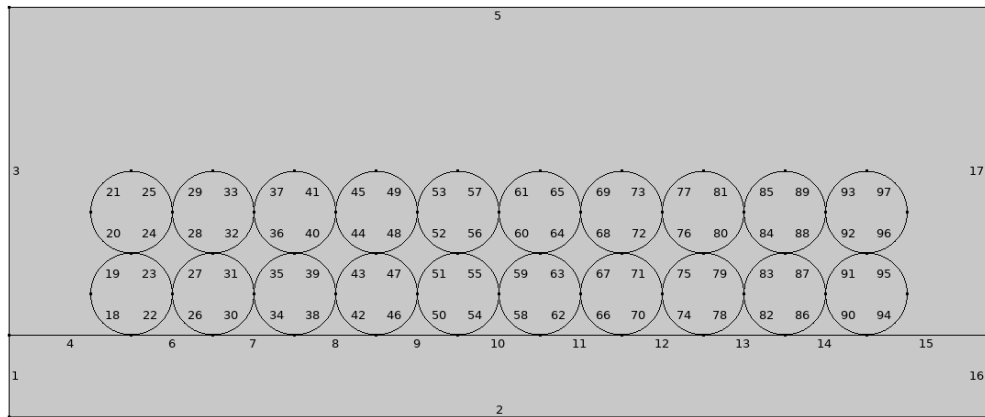


Figure 4.2: Particle bed geometry with labeled boundaries.

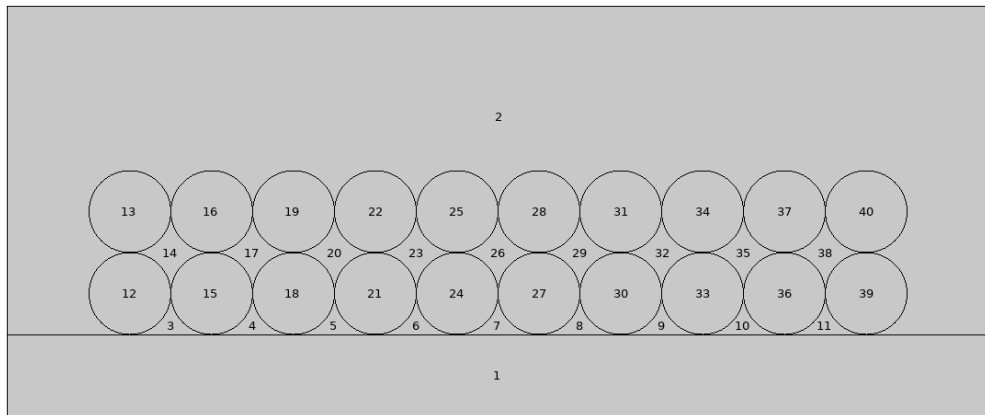


Figure 4.3: Particle bed geometry with labeled domains.

Laminar Flow

1. Open the **Physics** tab in the COMSOL GUI.
2. Right-click on **Component 1** → **Add Physics**. Add the **Laminar Flow** physics interface.
3. Click on the **Laminar flow** settings.
4. Under **Physical Model**, set the **Compressibility** to **Incompressible flow**.
5. Check the box for **Include gravity**.
6. Under **Consistent Stabilization**, check the boxes for **Streamline diffusion**, **Crosswind diffusion**, and **Use dynamic subgrid time scale**.
7. Under **Inconsistent Stabilization**, check the box for **Isotropic diffusion**.

Set the tuning parameter to 0.25. We are not interested in turbulent phenomena in the air domain above our particle bed, so the artificial diffusion is acceptable for our model.

8. Under **Discretization**, set the **Discretization of fluids** to P3+P2. This uses cubic shape functions for the velocity field and quadratic shape functions for the pressure field.
9. Under **Dependent Variables**, set the names of the **Velocity field components** to u, v, and w. and set the name of the **Pressure** to p. This is important for compatibility with our previous variable definitions.
10. Navigate to the **Fluid Properties** node.
11. Set the density to the variable **rho**.
12. For constitutive relation, choose specify dynamic viscosity.
13. Set the viscosity to the variable **mu**.
14. Navigate to **Initial Values**.
15. Set the velocity components to zero and set the pressure to 1 [atm].
16. Uncheck the box that says **Compensate for hydrostatic pressure**.
17. Under the **Laminar Flow** interface, right-click and select **Volume Force**.
18. In the **Volume Force** settings, ensure the **Selection** is set to **All Domains**.
19. Set the x and y components of **Volume Force** to **Fstx** and **Fsty**.
20. Right-click on the **Laminar Flow** interface in the **Model Builder**.
21. Select the **Outlet** boundary condition.
22. In the **Outlet** settings, select **Boundary 5** as seen in Figure 4.2.
23. Choose the **Boundary Condition** as pressure and set the pressure to 1 [atm].

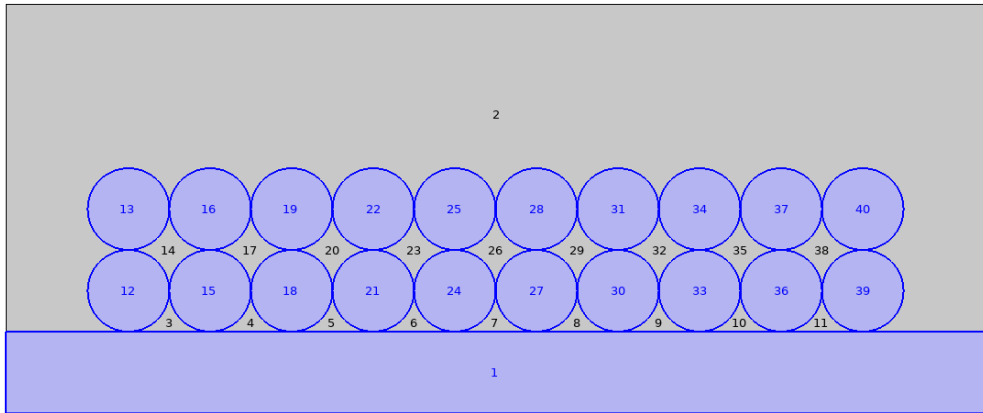


Figure 4.4: Ensure that for the phase field interface, the following domains are included in the selection for the `Initial Values, Fluid 2` node.

Phase Field

1. Right-click on `Component 1` → `Add Physics` and choose the `Phase Field` physics interface.
2. Click on the `Phase Field Interface` settings.
3. Under `Advanced Settings`, set the `Convective form` to `Nonconservative form`.
4. Under `Discretization`, set the `Element order` to `Quadratic`. Check both the boxes for `Compute boundary fluxes` and `Apply smoothing to boundary fluxes`.
5. Under `Dependent Variables`, set the names of the `Dependent Variables` as follows. Set the name of the `Phase field variable` to `phipf`, `Phase field help variable` to `psi`, and `Reciprocal initial interface distance` to `GI`. This is important in order to make the equations compatible with our previous variable declarations.
6. Navigate to `Phase Field` → `Phase Field Model`.
7. Set the `Surface Tension` to the variable `sigma`.
8. Set the `Parameter controlling interface thickness` to `epsilon`.
9. Set the `Mobility tuning parameter` to 0.
10. In the `velocity field`, set the x and y components of to `u` and `v`.

11. Set the **Selection** for the **Initial Values**, **Fluid 2** feature to all domains except for Domain 2 as shown in Figures 4.3 and 4.4.
12. Right-click on the **Phase Field** interface and choose the **Outlet** boundary condition.
13. In the **Outlet** settings, set the **Boundary Selection** to **Boundary 5** as shown in Figure 4.2.

Heat Transfer in Fluids

1. Right-click on **Component 1** → **Add Physics** and add the **Heat Transfer in Fluids** physics interface.
2. Click on the **Heat Transfer in Fluids** Interface settings.
3. Under **Discretization**, set the **Element order** to **Linear**. Check both the boxes for **Compute boundary fluxes** and **Apply smoothing to boundary fluxes**.
4. Under **Dependent Variables**, set the name of the **Dependent Variable** to **T**. This is important in order to make the equations compatible with our previous variable declarations.
5. Navigate to the **Fluid** node.
6. Set the velocity field to **u** and **v** respectively.
7. Set the thermal conductivity to the variable **k**.
8. Set the fluid type to **Gas/Liquid**.
9. Set the density to the variable **rho**.
10. Set the specific heat to the variable **Cp**.
11. Right-click on **Heat Transfer in Fluids** → **Heat Source**, to add the **Heat Source 1** node.
12. In the **Heat Source 1** settings, set the **Selection** to all domains.
13. Set the **Material type** as **Nonsolid**.
14. Set the **Heat source** to be **General source** and set Q_0 to be the variable **Qlaser**.
15. Right-click on **Heat Transfer in Fluids** → **Heat Source**, to add the **Heat Source 2** node.
16. In the **Heat Source 2** settings, set the **Selection** to all domains.

17. Set the **Material type** as **Nonsolid**.
18. Set the **Heat source** to be **General source** and set Q_0 to be the variable **Qr**.
19. Right-click on **Heat Transfer in Fluids** → **Heat Flux** to add the **Heat Flux 1** node.
20. In the **Heat Flux 1** settings, set the **Selection** to **All Boundaries**.
21. Set the material type to **Nonsolid**.
22. Set the **Flux type** to **General inward heat flux**.
23. Set q_0 to $k*(T_{amb} - T) / dwidth$.

Radiative Transfer Equation

1. Right-click on **Component 1** → **Add Physics** and add the **Poisson Equation** physics interface.
2. Click on the **Poisson Equation Interface** settings.
3. Under **Discretization**, set the **Shape function type** to **Lagrange**. Set the **Element order** to **Linear**. Check both the boxes for **Compute boundary fluxes** and **Apply smoothing to boundary fluxes**.
4. Under **Dependent Variables**, set the name of the **Dependent Variable** to **Grad**. This is important in order to make the equations compatible with our previous variable declarations.
5. Navigate to the **Poisson Equation 1** node.
6. Set the diffusion coefficient c to **Dp1**.
7. Set the source term f to **-Qr**.
8. Under **Units**, set the unit of the **Dependent variable quantity** to **$W*m^{-2}$** .
9. Under **Units**, set the unit of the **Source term quantity** to **$W*m^{-3}$** .
10. Right-click on **Poisson Equation** and add a **Flux** boundary condition.
11. In the **Flux Boundary** settings, set the **Boundary Selection** to **All Boundaries**.
12. Under **Boundary Flux/Source** set g to $0.5*(4*pi*Ib - Grad)$.
13. Under **Boundary Absorption/Impedance Term** set q to 0.

Mesh Settings

1. Navigate to **Mesh 1**. Clear any previous configurations.
2. Right-click **Mesh 1** → **Free Triangular** to add free triangular mesh elements.
3. Right-click on **Free Triangular 1** → **Size** in order to add a **Size** node.
4. Click on the **Size** node settings.
5. Under **Element Size Parameters**, set **Maximum element size** to $0.5*D$. Set **Minimum element size** to $0.25*D$. Set the **Maximum element growth rate** to 0.5 .
5. Set **Curvature factor** to 0.5 . Set **Resolution of narrow edges** to 0.1 .

Study Settings

1. Right-click the root node of the model and select **Add Study**.
2. Select the **Time-Dependent with Phase Initialization** study.
3. Right-click **Study 1** → **Show Default Solver**.
4. For our simulations, we keep most of the default solver configurations. The only setting we change is in **Solver Configurations** → **Solution 1** → **Time-Dependent Solver 1.1**.
5. Under **Time-Stepping**, set the **Maximum step constraint** to **Constant**. Set the **Maximum Step** to 0.001 .

4.2.2 SLS Implementation with PA12

The finite element implementation with Nylon is very similar to that of Molybdenum. One of the main differences is that the materials properties are specified using the interpolation with data from the literature. See Chapter 3 for details on the materials data used with the PA12 simulations. The other difference is that instead of using a Newtonian constitutive relation, we use the viscoelastic relation of Equation 3.2. For more details on the implementation, see the code `Polyamide2DModel.java` on the Github at <https://github.com/finalbossqc/SLS>.

Chapter 5

Results

5.1 Molybdenum

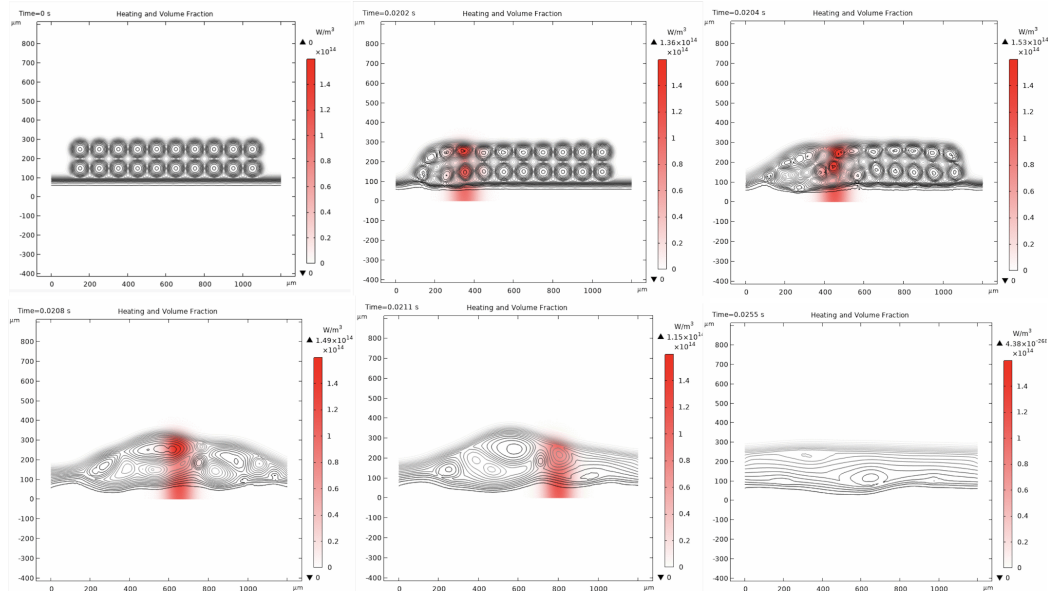


Figure 5.1: Heating profile of laser on Molybdenum with volume fraction isocontours. $D = 100 \mu\text{m}$, 20 particles total. $v_{\text{laser}} = 500 \text{ mm/s}$, $E_p = 300 \text{ W}$, and a laser penetration of $500 \mu\text{m}$

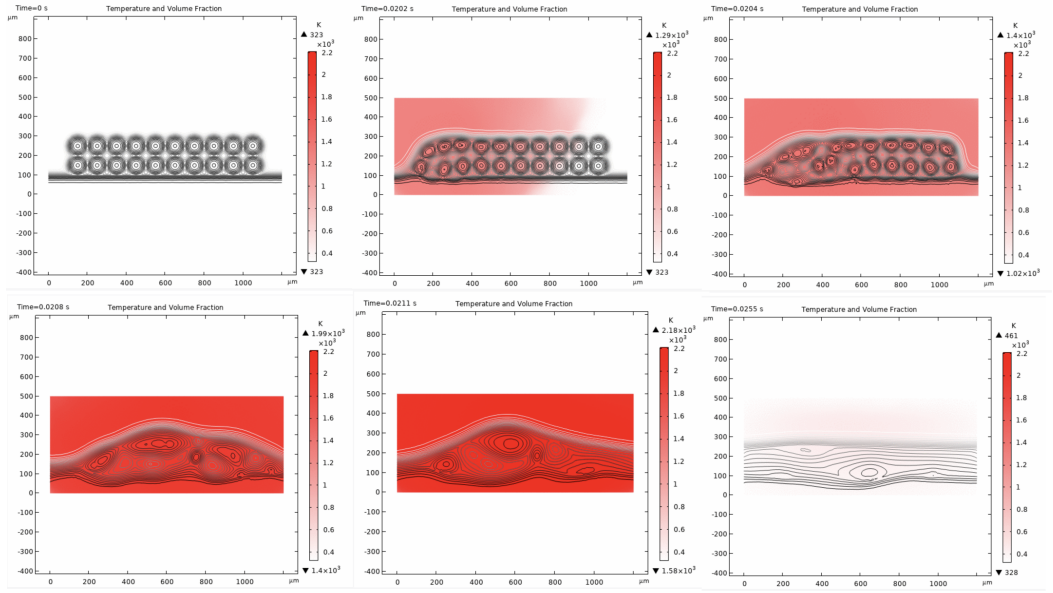


Figure 5.2: Temperature profile of laser on Molybdenum with volume fraction isocontours. $D = 100 \mu\text{m}$, 20 particles total. $v_{\text{laser}} = 500 \text{ mm/s}$, $E_p = 300 \text{ W}$, $r_{\text{laser}} = 50 \mu\text{m}$ and a laser penetration of $500 \mu\text{m}$

For all the simulations, we chose to use the value $d_{\text{width}} = 100 \mu\text{m}$ and to vary the laser power, laser speed, and laser penetration depth, first while keeping the particle size constant at $D = 100 \mu\text{m}$. Figures 5.1 and 5.2 show the laser heating and temperature profiles of a simulation with a laser penetration depth of $500 \mu\text{m}$. We observe a complete melt with a laser power of 300 W with no air bubbles trapped after 0.04 seconds of elapsed time. There are small irregularities in the solidified Molybdenum, but all air bubbles have been released during the melting and coalescence.

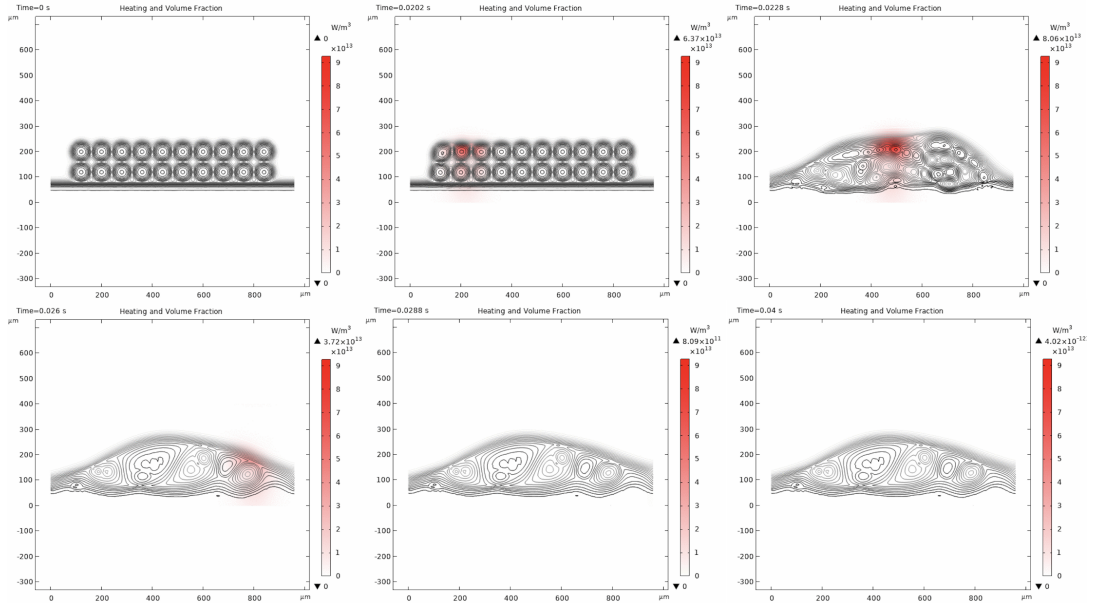


Figure 5.3: Heating profile of laser on Molybdenum with volume fraction isocontours. $D = 80 \mu\text{m}$, 20 particles total. $v_{\text{laser}} = 100 \text{ mm/s}$, $E_p = 150 \text{ W}$, and a laser penetration of $80 \mu\text{m}$

Then, we opted to change the particle size to observe changes in the melt dynamics. When we run the simulation with $D = 80 \mu\text{m}$, $E_p = 150 \text{ W}$ and $v_{\text{laser}} = 100 \text{ mm/s}$, we do see the trapping of air bubbles. As shown in Figures 5.3 and 5.4 of the heating and temperature profiles respectively, the air bubble fails to escape during the coalescence and is trapped well after the laser's heating has been turned off.

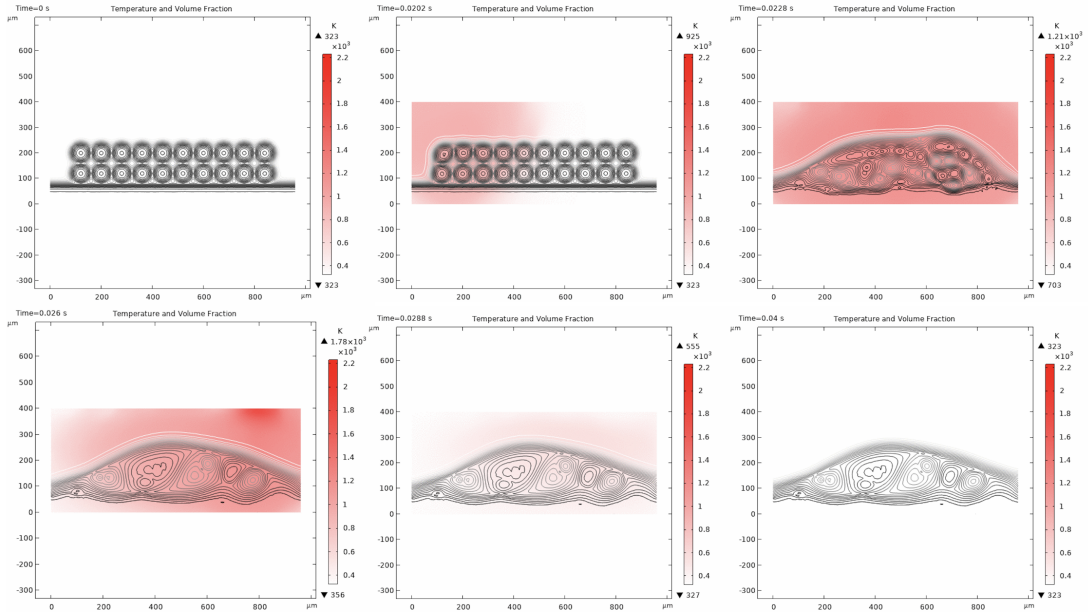


Figure 5.4: Temperature profile of laser on Molybdenum with volume fraction isocontours. $D = 80 \mu\text{m}$, 20 particles total. $v_{\text{laser}} = 100 \text{ mm/s}$, $E_p = 150 \text{ W}$, and a laser penetration of $80 \mu\text{m}$

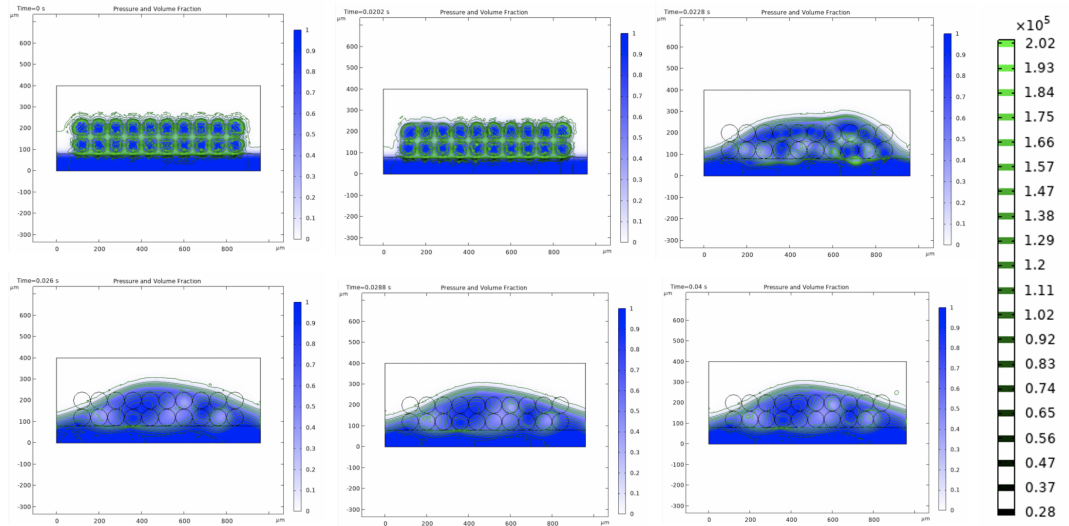


Figure 5.5: Volume fraction and pressure isocontours of Molybdenum. $D = 80 \mu\text{m}$, 20 particles total. $v_{\text{laser}} = 100 \text{ mm/s}$, $E_p = 150 \text{ W}$, and a laser penetration of $80 \mu\text{m}$

The air bubbles are more visible in Figure 5.5, which shows the volume fraction with pressure isocontours (pressure is measured in Pa). At 0.0228 s , some of the inner air bubbles are coalescing, but after the material cools, they remain trapped.

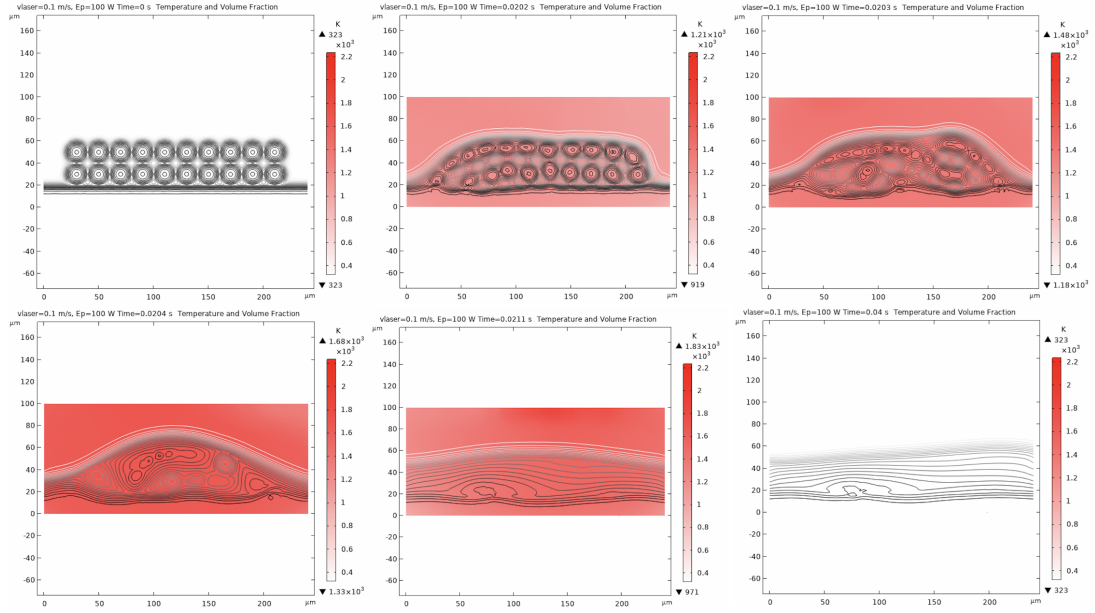


Figure 5.6: Temperature profile of Molybdenum $D = 20 \mu\text{m}$, 20 particles total. $v_{\text{laser}} = 100 \text{ mm/s}$, $E_p = 100 \text{ W}$, and a laser penetration of $80 \mu\text{m}$

By comparison, we lowered the particle size to $D = 20 \mu\text{m}$ and noticed that even with the same laser speed as before and a lower laser power of $E_p = 100 \text{ W}$, a complete melt is observed. Figures 5.6 and 5.7 show the temperature profile and volume fraction respectively, illustrating how the air bubbles are liberated despite a lower heating rate.

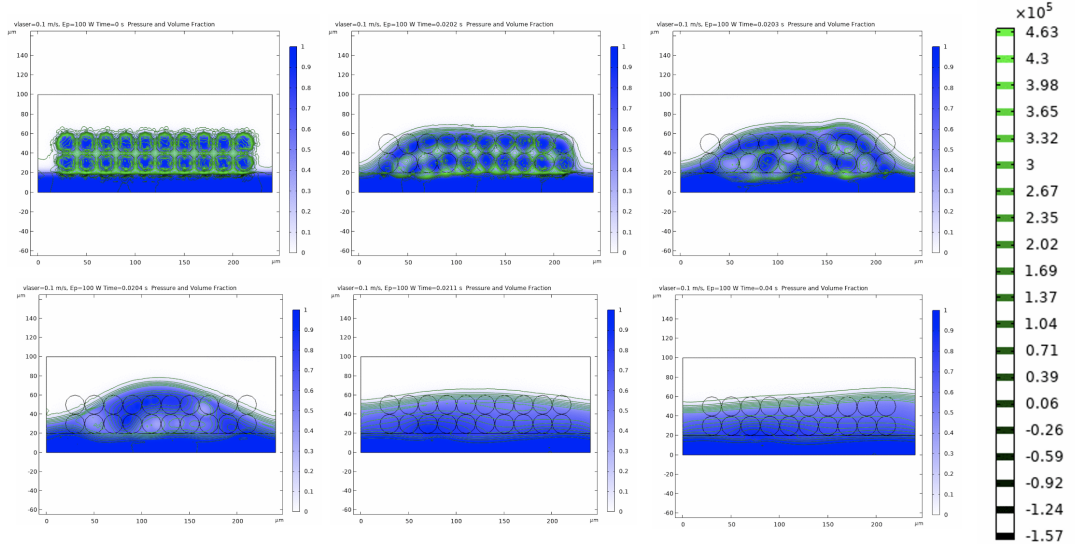


Figure 5.7: Volume fraction and pressure isocontours of Molybdenum. $D = 20 \mu\text{m}$, 20 particles total. $v_{\text{laser}} = 100 \text{ mm/s}$, $E_p = 100 \text{ W}$, and a laser penetration of $80 \mu\text{m}$

We explore the parameter space more thoroughly by sweeping over E_p and v_{laser} for different particle sizes. For particle size $D = 100 \mu m$, we observe Figure 5.8 to have complete melting only for $0.1 m/s$ at 200 and $250 W$. By comparison, we notice that for the sweeps with $D = 80 \mu m$, shown in Figure 5.9, more melting and coalescence are observed than with the $D = 100 \mu m$, suggesting that a smaller particle size is favorable for the formation of higher purity printed parts.

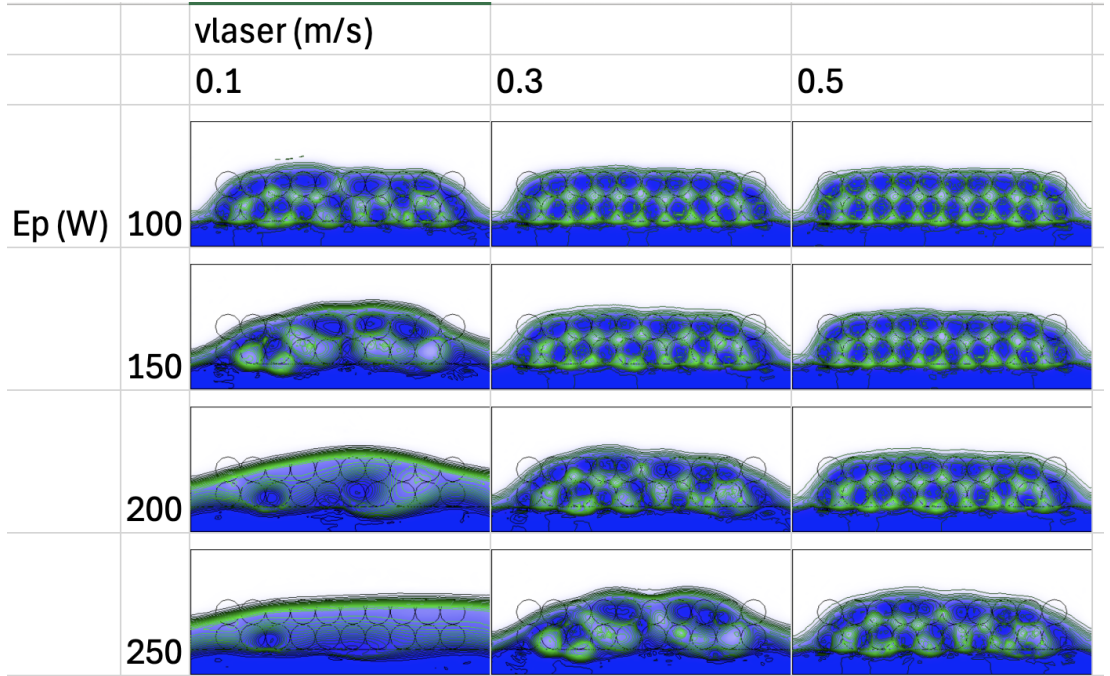


Figure 5.8: Process dynamics of Molybdenum. $D = 100 \mu m$, 20 particles total, and a laser penetration of $100 \mu m$ after $0.04 s$ of elapsed time.

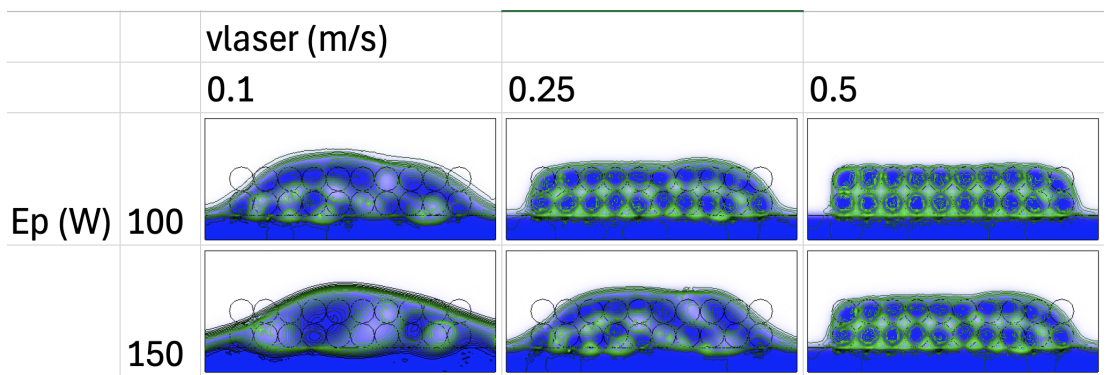


Figure 5.9: Process dynamics of Molybdenum. $D = 80 \mu m$, 20 particles total, and a laser penetration of $100 \mu m$ after $0.04 s$ of elapsed time.

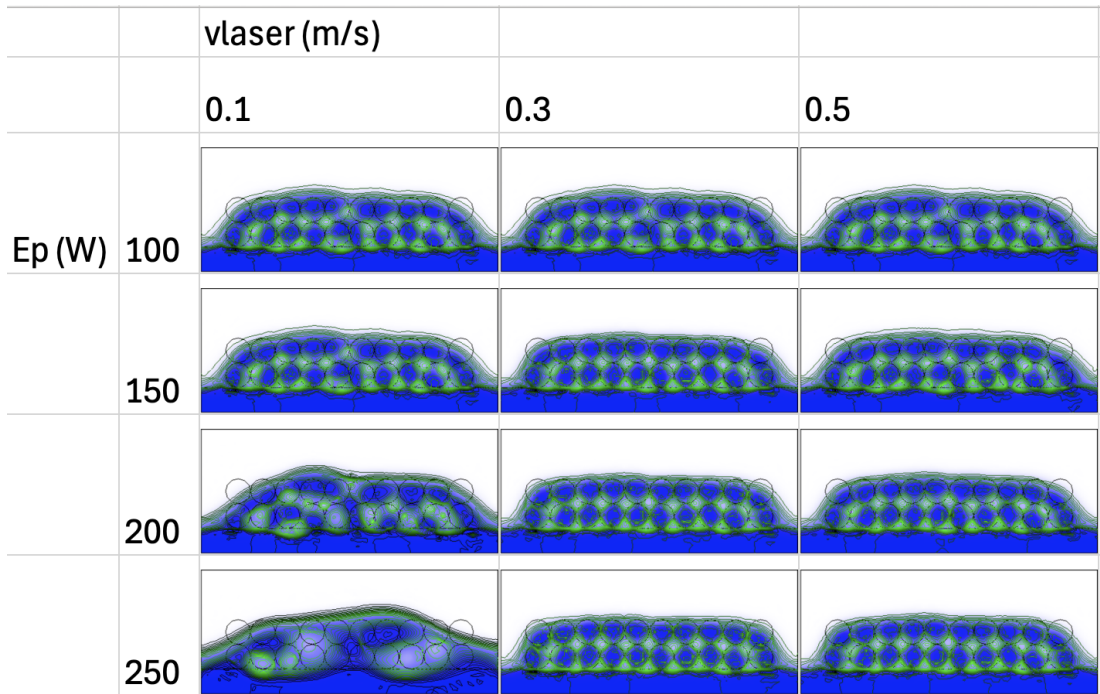


Figure 5.10: Process dynamics of Molybdenum. $D = 100 \mu\text{m}$, 20 particles total, and a laser penetration of $50 \mu\text{m}$ after 0.04 s of elapsed time.

We also notice from Figure 5.10 that when the laser penetration depth is half the particle size, very little melting occurs for all tested laser powers. The most melting and deformation of the powder bed occurs for 250 W at a laser speed of 100 mm/s .

5.2 PA12

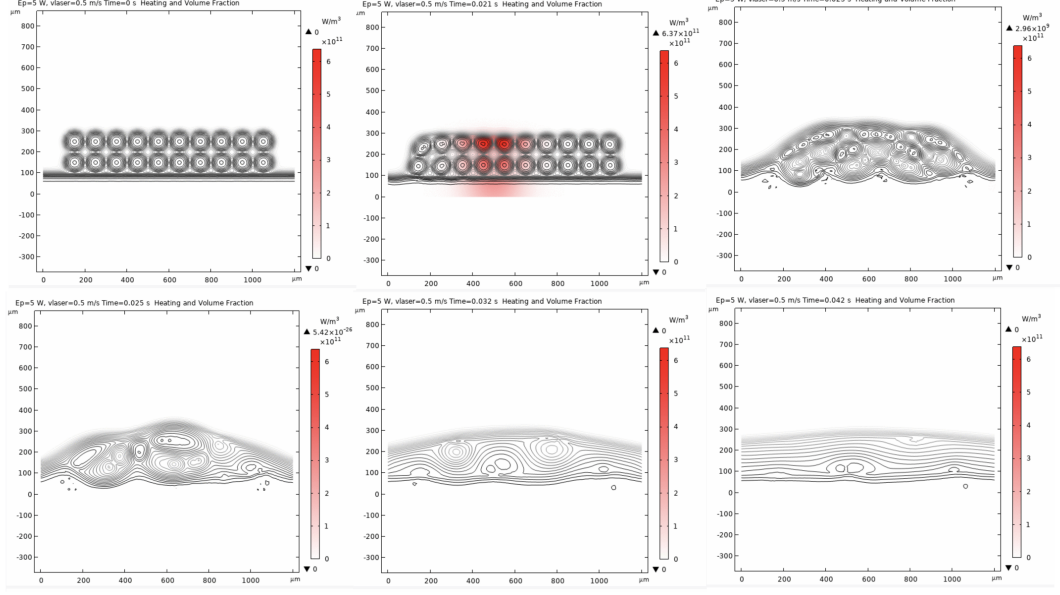


Figure 5.11: Heating profile of PA12. $D = 100 \mu\text{m}$, 20 particles total. $v_{laser} = 500 \text{ mm/s}$, $E_p = 5 \text{ W}$, and a laser penetration of $500 \mu\text{m}$

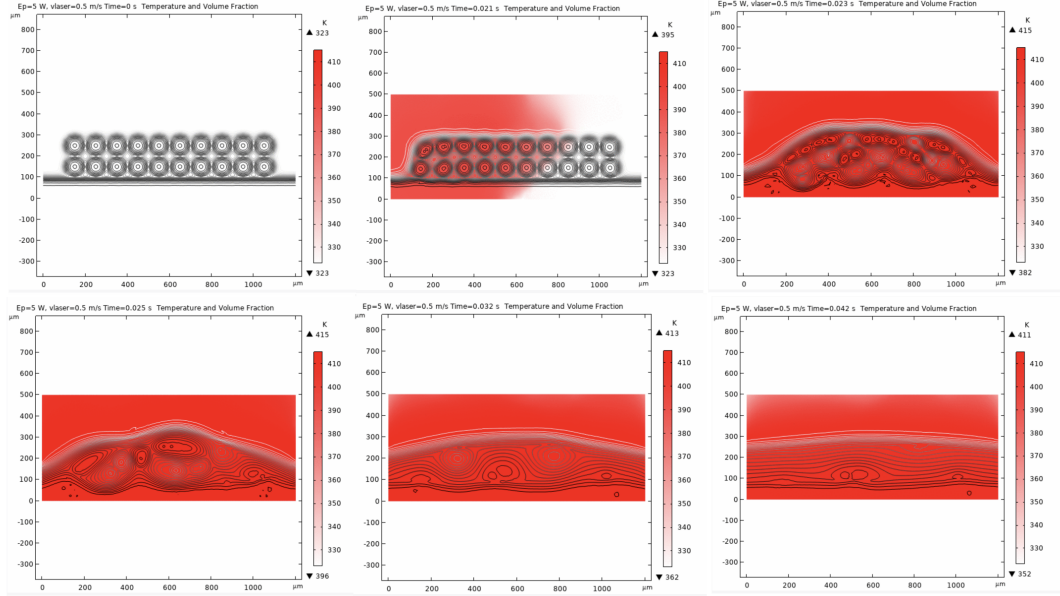


Figure 5.12: Temperature profile of PA12. $D = 100 \mu\text{m}$, 20 particles total. $v_{laser} = 500 \text{ mm/s}$, $E_p = 5 \text{ W}$, and a laser penetration of $500 \mu\text{m}$

For PA12, we do a similar initial analysis. From Figures 5.11 and 5.12, which depict the heating profile and the temperature profile respectively, we see that when $D = 100$

μm , $v_{laser} = 500 \text{ mm/s}$ and $E_p = 5 \text{ W}$, we have complete melting of the polymer. An important difference from the Molybdenum simulations is that the PA12 simulations take longer to cool due to the lower thermal conductivity of PA12 compared to Molybdenum.

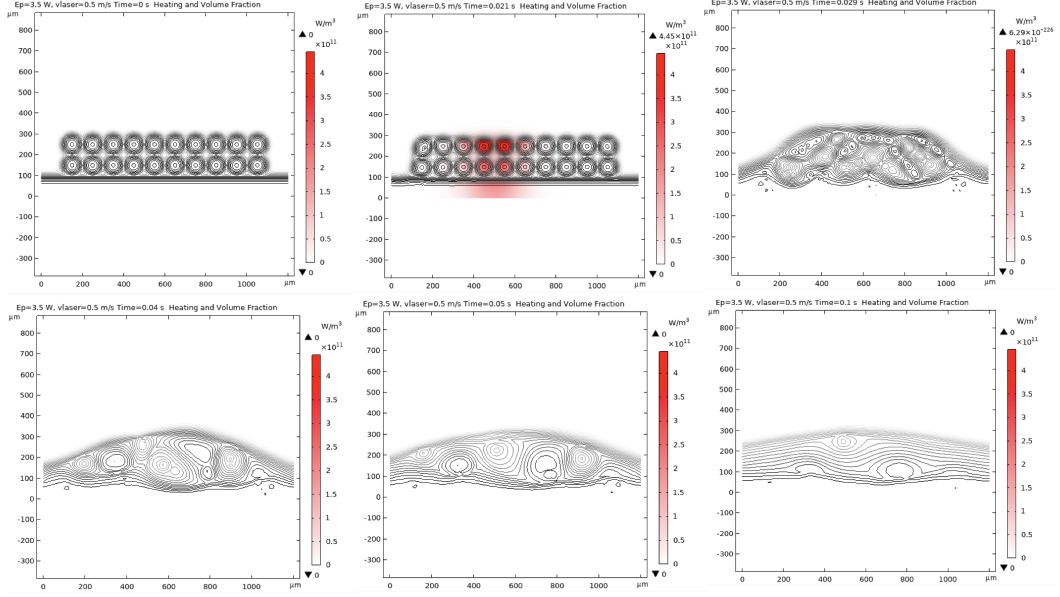


Figure 5.13: Heating profile of PA12. $D = 100 \mu\text{m}$, 20 particles total. $v_{laser} = 500 \text{ mm/s}$, $E_p = 3.5 \text{ W}$, and a laser penetration of $500 \mu\text{m}$

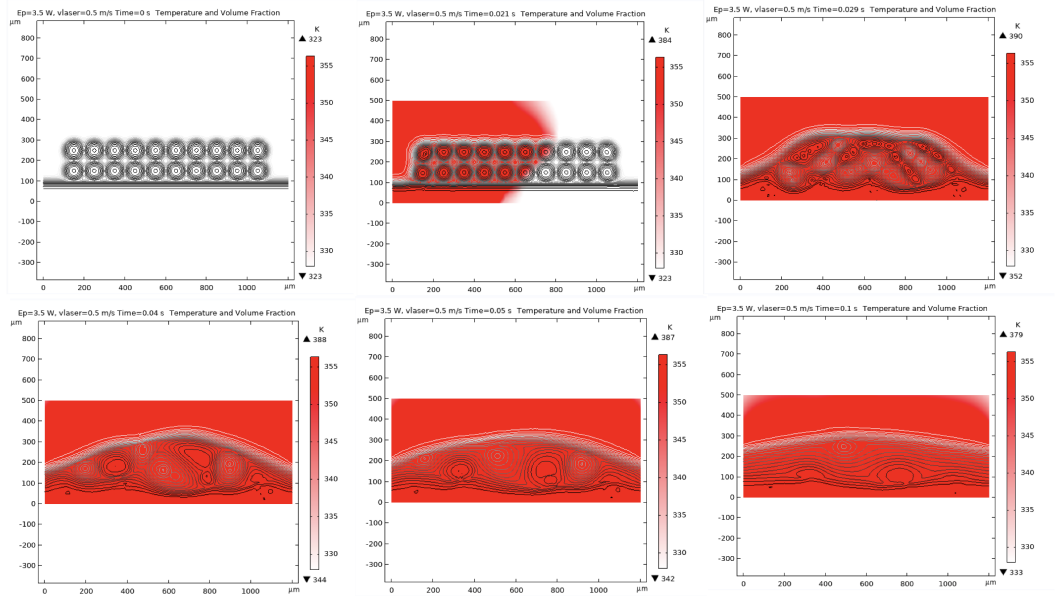


Figure 5.14: Temperature profile of PA12. $D = 100 \mu\text{m}$, 20 particles total. $v_{laser} = 500 \text{ mm/s}$, $E_p = 3.5 \text{ W}$, and a laser penetration of $500 \mu\text{m}$

We try a similar experiment, but we only change the laser power to $E_p = 3.5 \text{ W}$, and we can see from Figures 5.13 and 5.14 that the sample is not as uniform. By 0.1 s, there is an air bubble in the process of escaping, but the bubble is not completely frozen out.

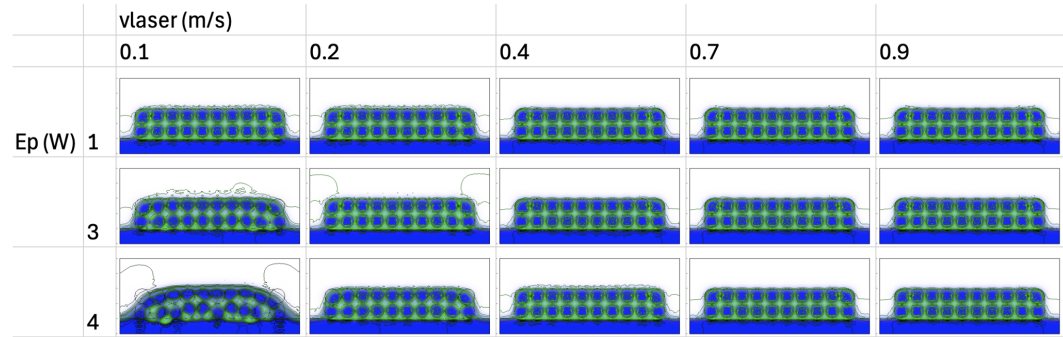


Figure 5.15: Process dynamics of Polyamide. $D = 100\mu\text{m}$, 20 particles total, and a laser penetration of $50 \mu\text{m}$ after 0.1 seconds of elapsed time.

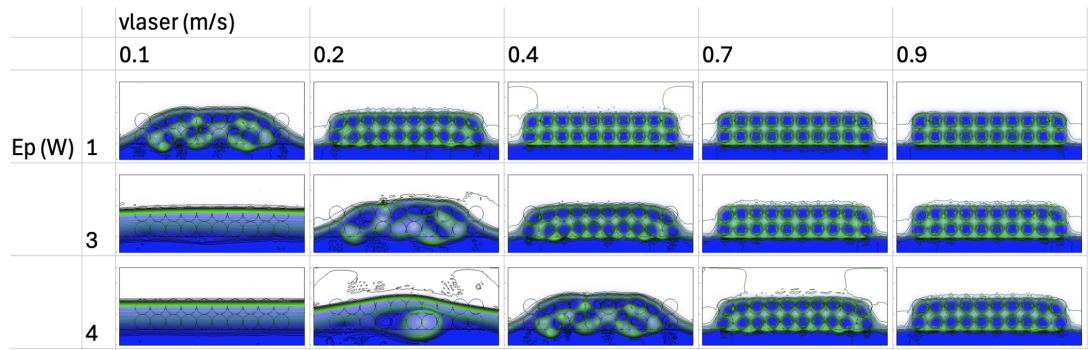


Figure 5.16: Process dynamics of Polyamide. $D = 100\mu\text{m}$, 20 particles total, and a laser penetration of $100 \mu\text{m}$ after 0.1 seconds of elapsed time.

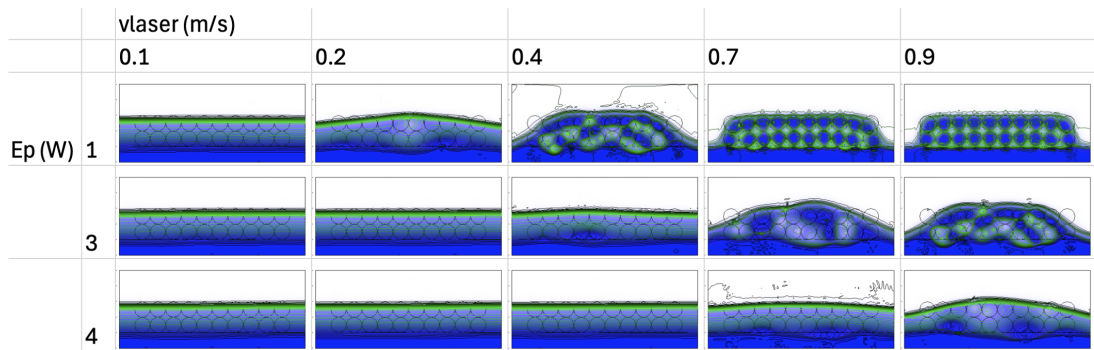


Figure 5.17: Process dynamics of Polyamide. $D = 100\mu\text{m}$, 20 particles total, and a laser penetration of $300 \mu\text{m}$ after 0.1 seconds of elapsed time.

The trends in process dynamics are similar to those of Molybdenum. As seen in Figure 5.15, when the penetration depth is $50 \mu\text{m}$, there is minimal melting across all laser powers and laser speeds. By contrast, Figures 5.16 and 5.17 show that with increased penetration depth, the laser melting occurs at both lower E_p and higher v_{laser} .

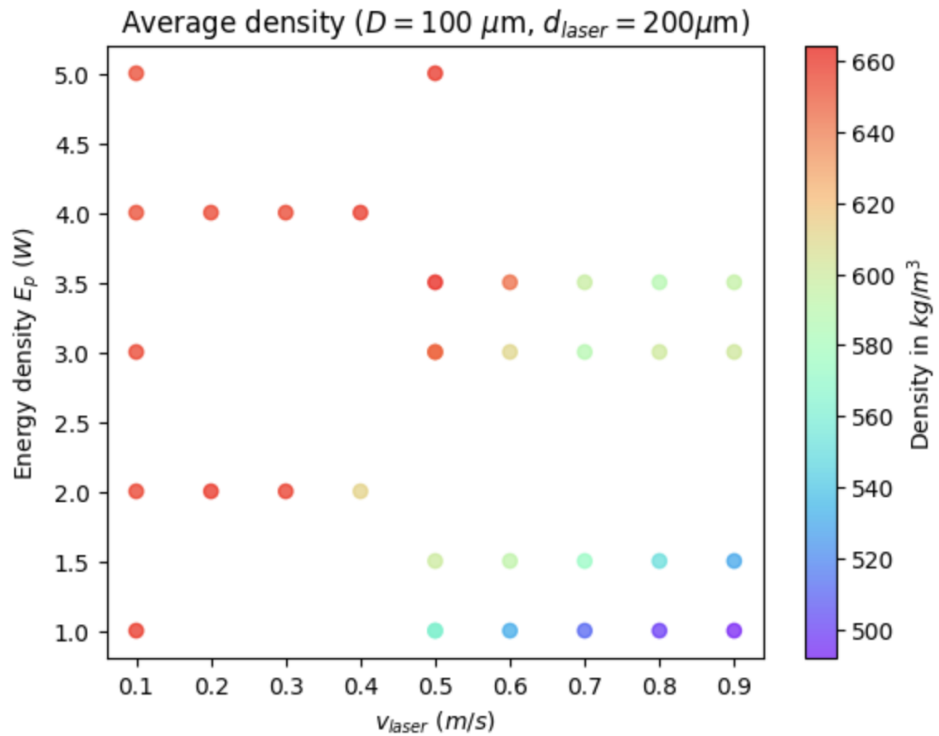


Figure 5.18: A plot of the average density of the printed PA12 part when the penetration depth of the laser was $200 \mu\text{m}$. The density measurements were taken 0.1 seconds after the start of the simulation.

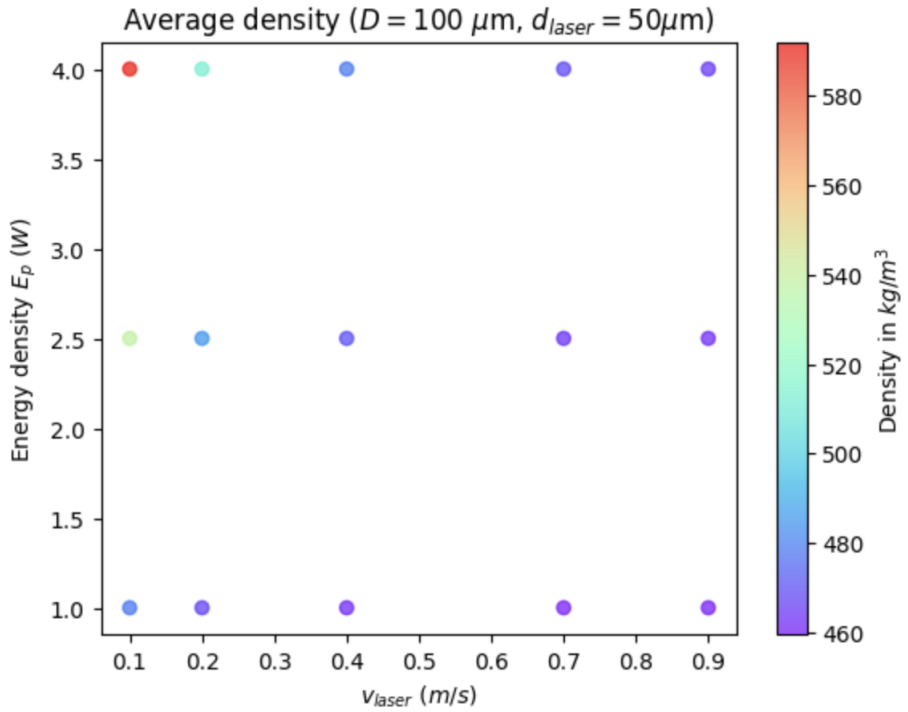


Figure 5.19: A plot of the average density of the printed PA12 part when the penetration depth of the laser was $200 \mu\text{m}$. The density measurements were taken 0.1 seconds after the start of the simulation.

The process dynamics are also illustrated in Figures 5.18 and 5.19. For the simulations with laser penetration of $d_{laser} = 200 \mu\text{m}$, the region of complete melting corresponds to a density of approximately 660 kg/m^3 . By comparison, the simulations with $d_{laser} = 50 \mu\text{m}$ show a lower average density across all combinations of E_p and v_{laser} .

Another parameter that can affect the process dynamics and the development of impurities in the simulations is the interface thickness of the phase field model ϵ . For all the previous simulations with Molybdenum and PA12, the interface thickness used was $\epsilon = 0.15D$, meaning that the size of the interface between air and the powder material is 15% of the diameter of the initial powder particles. The interface thickness accounts for uncertainty in the phase, allowing for simpler computation, but we can also use sharper interfaces to get more accurate simulation of the interfacial dynamics.

We try a simulation with $E_p = 3 \text{ W}$ and $v_{laser} = 100 \text{ mm/s}$ and $d_{laser} = 100 \mu\text{m}$ to show the differences in bubble formation due to a sharp interface of $\epsilon = 0.1D$. As we see in Figures 5.20 there is a clear difference in the release of the bubbles. Whereas previous simulations showed smaller bubbles, now the bubbles themselves coalesce together to form larger bubbles that take longer to leave the material.

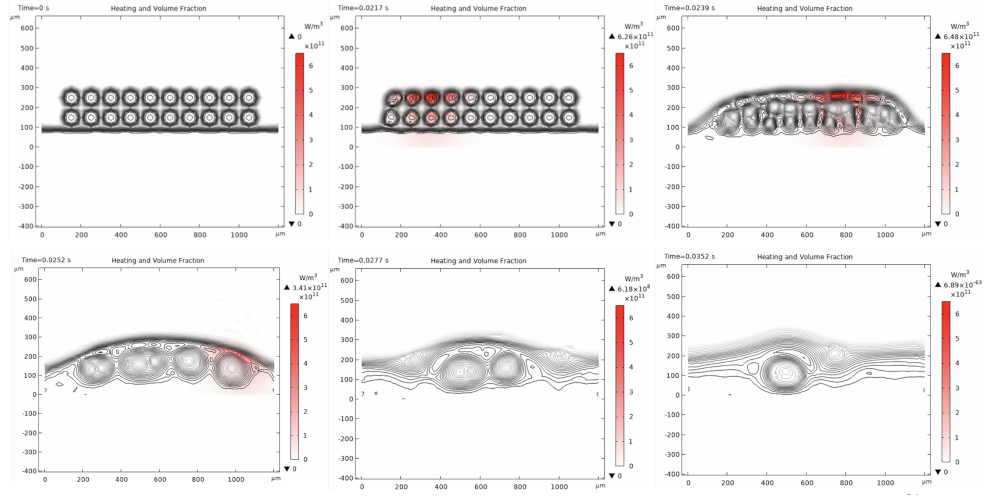


Figure 5.20: Heating profile of PA12. $D = 100 \mu\text{m}$, 20 particles total. $v_{\text{laser}} = 100 \text{ mm/s}$, $E_p = 3 \text{ W}$, a laser penetration of $100 \mu\text{m}$, and an interface thickness of $\epsilon = 0.1D$.

Chapter 6

Discussion

6.1 Comparison with Experiment

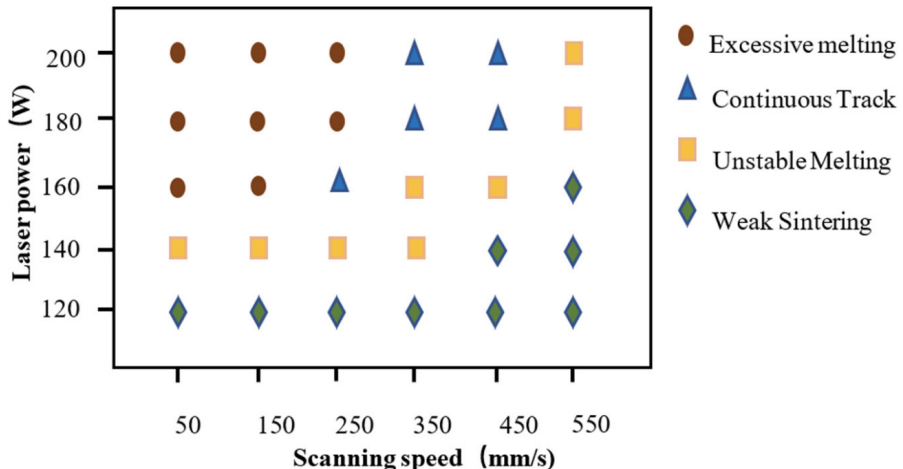


Figure 6.1: A figure taken from a paper by Yan et al. 2022 that showcases experimental results that highlight the process dynamics of SLS with Molybdenum

We can compare the process tables collected from our COMSOL simulations and notice similar trends. The process window in which the highest quality parts are obtained resides near higher laser powers and lower scanning speeds. If we compare Figure 6.1 to Figure 5.8 on a case by case basis, we see some striking similarities in the process dynamics. At 500 mm/s both the COMSOL result and the experimental result exhibit weak melting and little deformation of the air domains. At 100 mm/s in both the graph and the process table, we see total melting occurring at laser powers above 200

W and unstable melting occurring between 150 to 160 W .

It is important to note that Yan et al. 2022 does use smaller particles than the ones used in this simulation. This result seems to suggest that the laser penetration used in the experimental study was likely very close to the size of the particles, leading to similar coalescence patterns and melt dynamics.

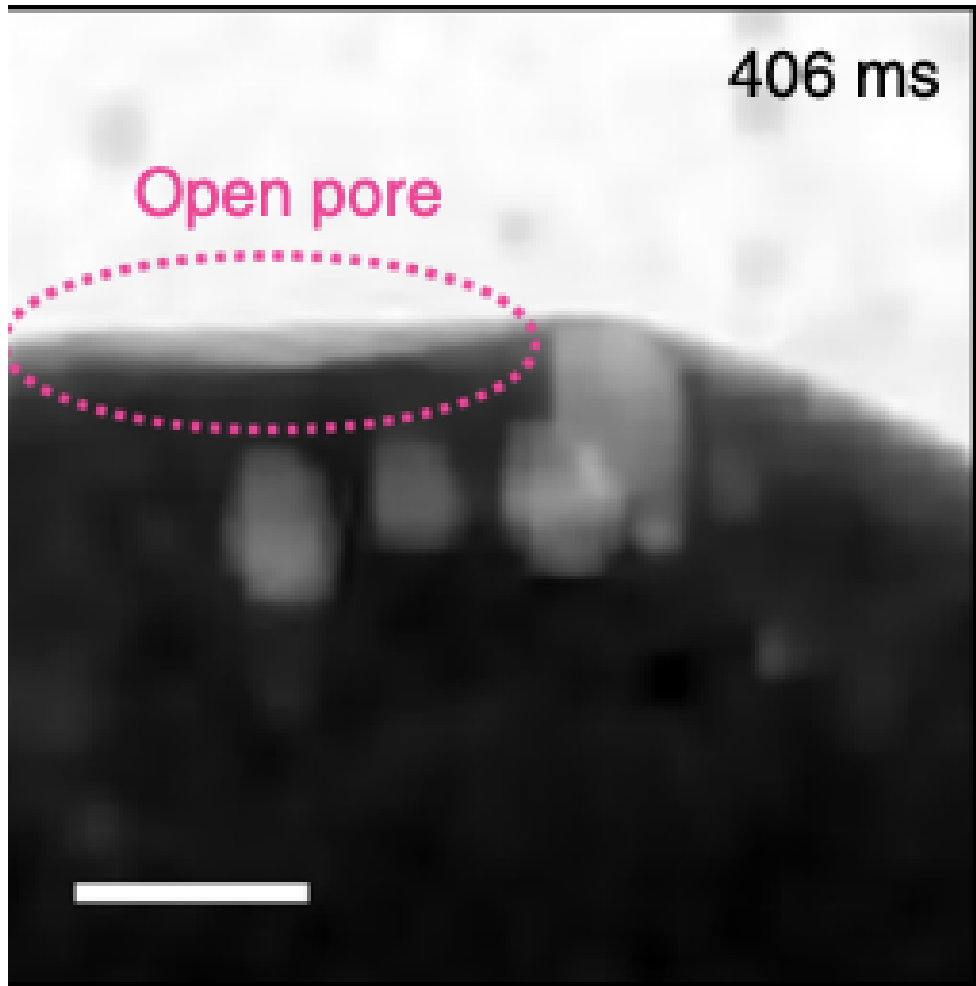


Figure 6.2: An image taken from a paper by Leung et al. 2018 that uses X-ray in situ imaging to observe an open pore near the interface of the air and material.

Leung et al. 2018 reports the observation of open pores during SLS, which is consistent with some of the COMSOL Molybdenum results. Referring back to Figure 5.8 the melt with parameters $E_p = 200 W$ and $v_{laser} = 0.1 m/s$ demonstrates an open pore similar to that shown in Figure 6.2 as well as other “frozen-in” pores. An open pore can also be observed in the Polyamide simulation in Figure 6.4.

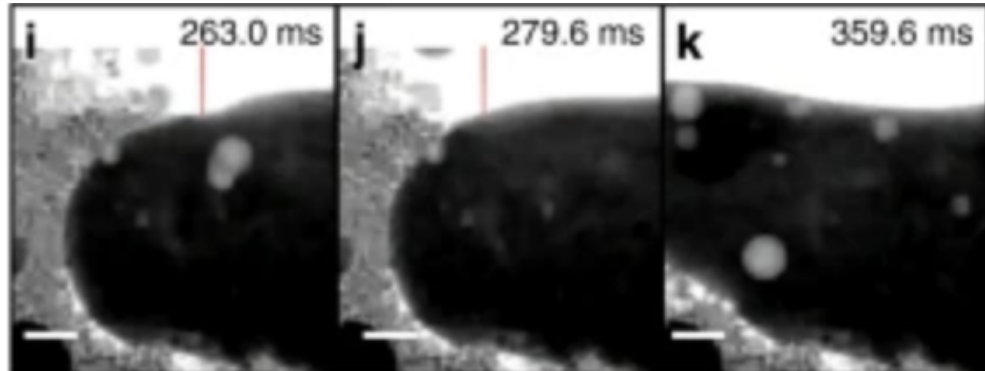


Figure 6.3: An X-ray image cross section showing bubbles during the sintering process (Leung et al. 2018)

Leung et al. 2018 also reports bubble formation during the melting as can be seen in Figure 6.3. This type of bubble flow can also be observed in Figure 5.7, where the bubbles quickly gather at the surface and diffuse into the surrounding air.

Another phenomena recorded by Leung et al. 2018 is known as spatter, a process in which particle mass is ejected near the interface due to surface tension forces. Interestingly, our COMSOL model also demonstrates evidence of spatter in select simulations as can be seen from some of the process tables of PA12 such as Figure 5.16 with $E_p = 3 W$ and $v_{laser} = 0.2 m/s$ which demonstrates uncharacteristic behavior in the pressure isocontours after the release of a small bubble as shown more closely in Figure 6.4.

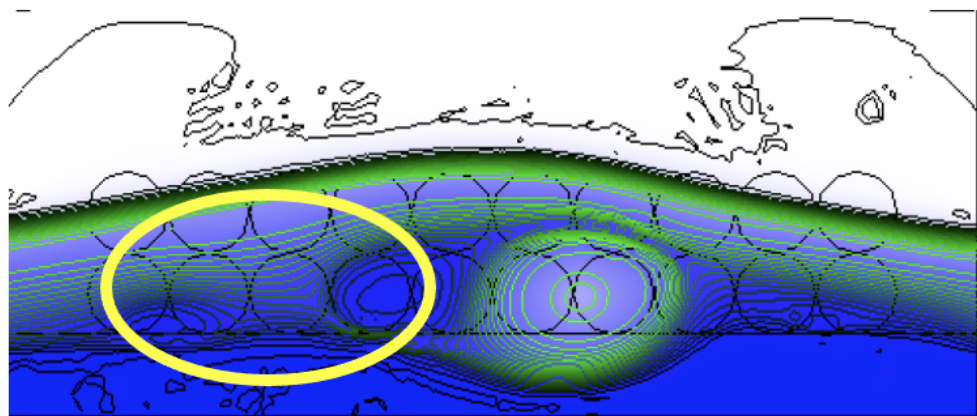


Figure 6.4: A simulation image of PA12 with an air bubble leaving the material and distorting the pressure isocontours. Highlighted is an open pore where an air bubble is accessible to the surface.

A similar evidence of spatter is also in Figure 5.16 with the parameter set $E_p = 3 W$ and $v_{laser} = 0.2 m/s$ as can be seen more closely in Figure 6.5. The pressure contours

shown here are noticeably distorted. This is not a normal phenomena that is seen across all the PA12 melts and the effect is not nearly as strong in any of the process tables of the Molybdenum melts. Thus, it is reasonable to conclude that the effects of spatter are a combination of surface tension effects and viscoelastic effects, which is why we observe spatter in our PA12 melts where we used a complex rheological model and not in Molybdenum where we used the Newtonian model.

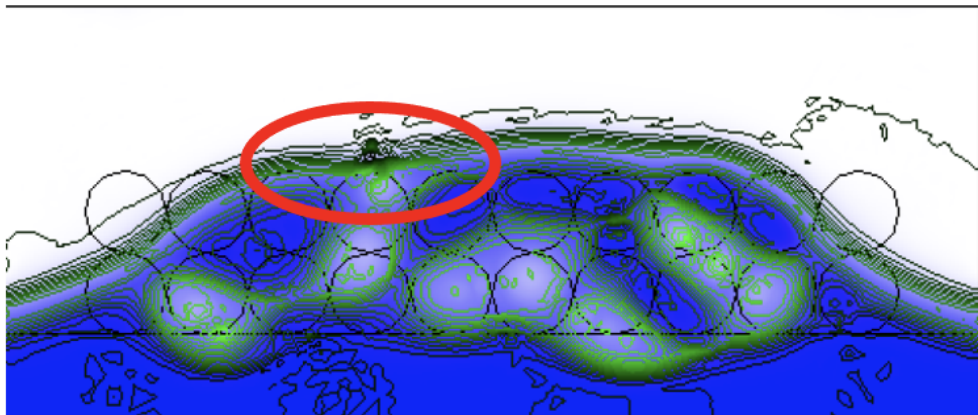


Figure 6.5: Highlighted image of spatter as the distortion and concentration of pressure isocontours occurs while a bubbles escapes.

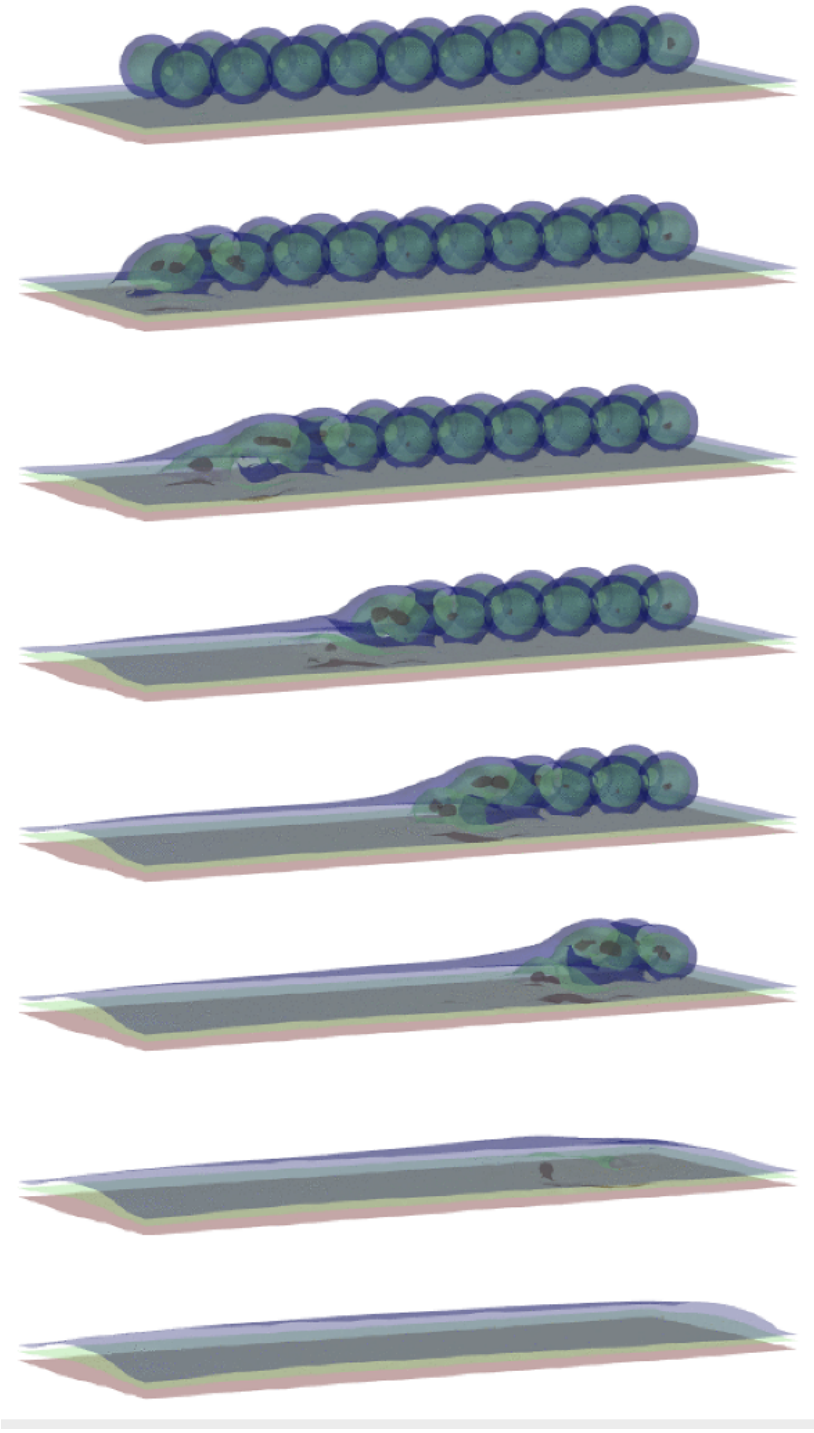


Figure 6.6: Time evolution of isosurfaces of volume fraction in 3D simulation of polyamide with laser power of 3 W and a laser speed of 0.1 m/s. The first image on the top shows the initial configuration of the particles (there are 20 particles) and each subsequent image is 0.001 seconds apart starting from the time the laser is turned on.

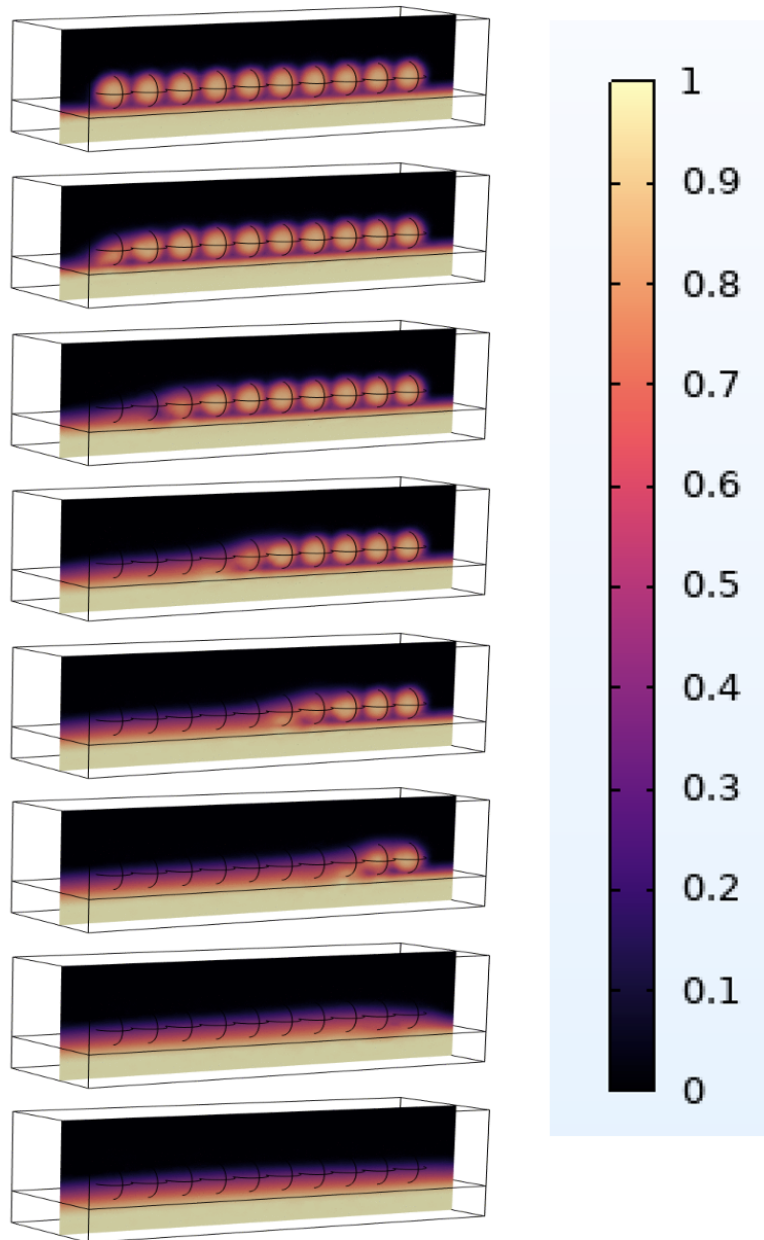


Figure 6.7: Time evolution of 2D cross sections of volume fraction in the 3D simulation of polyamide with laser power of 3 W and a laser speed of 0.1 m/s.

6.2 Comparison between 2D and 3D Results

In the 3D simulation results shown in Figure 6.6, we can see that the laser causes the particles to deform and fuse into the powder layer below it. With the 3 W laser on a single layer of particles, we see a complete melt as the material originally contained in

the particles is distributed over the previous layer. A cross section of the 3D result, shown in Figure 6.7, reveals a similar result to the 2D simulations, with the escaping of small bubbles as the laser runs over the material.

We can compare the 3D result to the 2D result with the same parameters as shown in Figure 6.8. The same laser power and laser speed also results in a complete melt in 2D, which indicates a consistent result with the 3D simulations.

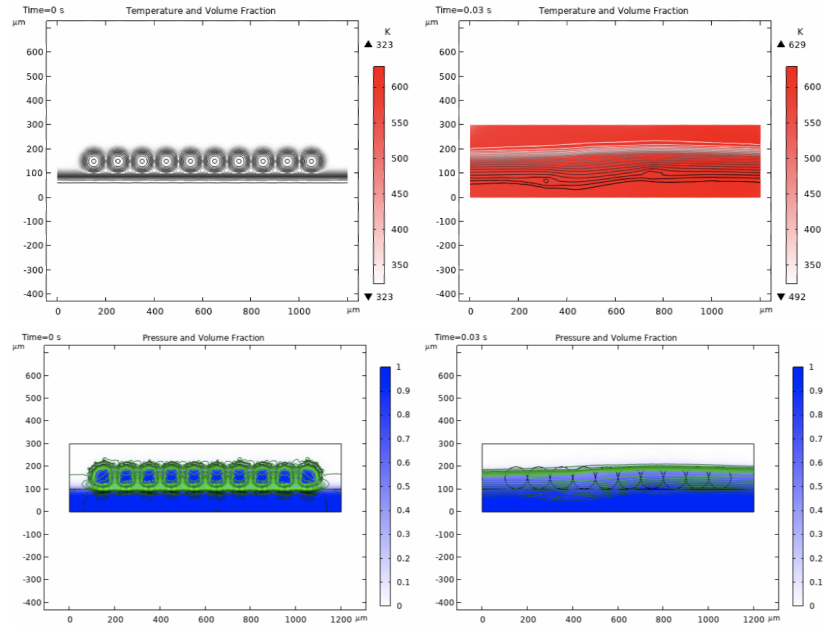


Figure 6.8: Melting of a single particle layer with a laser power of 3 W and a laser speed of 0.1 m/s. Shown are the temperature and volume fraction at $t = 0$ s and $t = 0.03$ s. Note that the laser is turned on at $t = 0.02$ s.

It is important to note that 2D models tend to underestimate the amount of energy needed to melt the material. In 3D, there is conduction and radiation occurring out of plane, which would not be accounted for in the 2D simulation.

6.3 Conclusion and Future Work

This study presented a detailed multiphysics simulation framework using COMSOL to investigate the selective laser sintering (SLS) of both metallic (Molybdenum) and polymeric (PA12) powders. The simulation results were validated against experimental data from the literature and exhibited strong qualitative agreement with respect to process dynamics such as melting behavior, pore formation, and spatter events. Notably, similar trends in the process window were observed, including the dependence of full

melting on high laser powers and low scanning speeds.

The emergence of open and “frozen-in” pores, bubble formation, and spatter phenomena in the COMSOL simulations further support the fidelity of the developed models. The inclusion of a viscoelastic rheological model for PA12 captured unique behaviors not seen in the Newtonian Molybdenum model, indicating that material properties significantly influence melt dynamics and defect formation.

A comparison between 2D and 3D simulations revealed that 2D models tend to underestimate the energy required for effective melting due to neglected out-of-plane thermal losses. This finding underscores the importance of full 3D simulations for accurate prediction of sintering quality, despite the higher computational cost.

Future work will focus on extending the current 3D modeling framework to incorporate full melt dynamics, surface tension effects, and accurate radiative heat transfer. Additionally, incorporating particle-scale resolution and stochastic packing arrangements could provide further insight into defect formation mechanisms and improve predictive accuracy. Experimental validation with in-house data and the integration of machine learning techniques to optimize process parameters also represent promising directions for continued research.

Bibliography

- Baturynska, Ivanna, Oleksandr Semeniuta, and Kjell Martinsen (2018). “Optimizing the 3D printing process by the application of fuzzy logic in ANN for the part built from polymer”. In: *Procedia CIRP* 67, pp. 498–503.
- Bejan, Adrian (Apr. 2013). *Convection Heat Transfer, 4th edition*. John Wiley #38; Sons, Inc. DOI: [10.1002/9781118671627](https://doi.org/10.1002/9781118671627). URL: <https://core.ac.uk/display/44363643>.
- Bodryakov, V Yu (2014). “Correlation of temperature dependencies of thermal expansion and heat capacity of refractory metal up to the melting point: Molybdenum”. In: *High temperature* 52.6, pp. 840–845.
- Charoo, Naseem A et al. (2020). “Selective laser sintering 3D printing—an overview of the technology and pharmaceutical applications”. In: *Drug development and industrial pharmacy* 46.6, pp. 869–877.
- Clijsters, Stijn et al. (2014). “In situ quality control of the selective laser melting process using a high-speed, real-time melt pool monitoring system”. In: *The International Journal of Advanced Manufacturing Technology* 75.5, pp. 1089–1101.
- Evans, Nathan T et al. (2015). “High-strength, surface-porous polyether-ether-ketone for load-bearing orthopedic implants”. In: *Acta biomaterialia* 13, pp. 159–167.
- Grasso, Marco and Bianca Maria Colosimo (2018). “In-process monitoring of selective laser melting: Spatial detection of defects via image data analysis”. In: *Journal of Manufacturing Science and Engineering* 139.5.
- Gu, Dongdong et al. (2017). “A multiscale understanding of the thermodynamic and kinetic mechanisms of laser additive manufacturing”. In: *Engineering* 3.5, pp. 675–684.
- He, Baizhen et al. (2024). “Influence of roughness and temperature on the emissivity of molybdenum in RTPV system”. In: *Materials Today Communications* 40, p. 110102.
- Kamath, Chandrika et al. (2016). “A review of predictive models for thermal properties and characteristics of the selective laser melting process”. In: *Additive Manufacturing* 12, pp. 61–76.

- Khairallah, Saad A et al. (2016). “Laser powder-bed fusion additive manufacturing: Physics of complex melt flow and formation mechanisms of pores, spatter, and denudation zones”. In: *Acta Materialia* 108, pp. 36–45.
- King, Wayne E et al. (2015). “Laser powder bed fusion additive manufacturing of metals; physics, computational, and materials challenges”. In: *Applied Physics Reviews* 2.4, p. 041304.
- Leitz, K-H et al. (2018). “Fundamental analysis of the influence of powder characteristics in Selective Laser Melting of molybdenum based on a multi-physical simulation model”. In: *International Journal of Refractory Metals and Hard Materials* 72, pp. 1–8.
- Leung, Chu Lun Alex et al. (2018). “In situ X-ray imaging of defect and molten pool dynamics in laser additive manufacturing”. In: *Nature communications* 9.1, p. 1355.
- Li, Jiang et al. (2020). “Numerical model and experimental validation for laser sinterable semi-crystalline polymer: shrinkage and warping”. In: *Polymers* 12.6, p. 1373.
- Li, Xiaopeng et al. (2018). “Thermal simulation of the cooling down of selective laser sintered parts in PA12”. In: *Rapid Prototyping Journal* 24.7, pp. 1117–1123.
- Lindemann, André and J Blumm (2009). *Measurement of the thermophysical properties of pure molybdenum*. na.
- Mielicki, C, B Gronhoff, and J Wortberg (2014). “Rheological changes of polyamide 12 under oscillatory shear”. In: *AIP Conference Proceedings*. Vol. 1593. 1. American Institute of Physics, pp. 231–235.
- Modest, Michael F and Sandip Mazumder (2021). *Radiative heat transfer*. Academic press.
- Mokrane, Amir, M'hamed Boudaous, and Shihe Xin (2018). “A computational framework for full-scale simulation of the selective laser sintering process: effect of scan pattern, laser power, and scan speed on the process”. In: *Journal of Manufacturing Science and Engineering* 140.11.
- Paradis, P-F, Takehiko Ishikawa, and Noriyuki Koike (2007). “Non-contact measurements of the surface tension and viscosity of molybdenum using an electrostatic levitation furnace”. In: *International Journal of Refractory Metals and Hard Materials* 25.1, pp. 95–100.
- Paradis, P-F, Takehiko Ishikawa, and Shinichi Yoda (2002). “Noncontact measurements of thermophysical properties of molybdenum at high temperatures”. In: *International journal of thermophysics* 23, pp. 555–569.
- Peltola, Matti J et al. (2012). “Novel composite implant in craniofacial bone reconstruction”. In: *European Archives of Oto-Rhino-Laryngology* 269, pp. 623–628.

- Peyre, Patrice et al. (2015). “Experimental and numerical analysis of the selective laser sintering (SLS) of PA12 and PEKK semi-crystalline polymers”. In: *Journal of Materials Processing Technology* 225, pp. 326–336.
- Rausch, Anne Marie et al. (2017). “Selective laser sintering of polymer powder of different particle rounding”. In: *Polymers* 9.4, p. 133.
- Robert, ERIC C et al. (2004). “Characterization of polyamides 6, 11, and 12. Determination of molecular weight by size exclusion chromatography (IUPAC Technical Report)”. In: *Pure and applied chemistry* 76.11, pp. 2009–2025.
- Sutton, Alexander T et al. (2017). “Powder characterisation for additive manufacturing processes”. In: *Virtual and Physical Prototyping* 12.1, pp. 3–29.
- Thompson, Mary Kathryn et al. (2016). “Design for additive manufacturing: Trends, opportunities, considerations, and constraints”. In: *CIRP annals* 65.2, pp. 737–760.
- Valverde, Israel et al. (2015). “3 D printed models for planning endovascular stenting in transverse aortic arch hypoplasia”. In: *Catheterization and Cardiovascular Interventions* 85.6, pp. 1006–1012.
- Vasco, Joel C (2021). “Additive manufacturing for the automotive industry”. In: *Additive Manufacturing*. Elsevier, pp. 505–530.
- Verbelen, Leander et al. (2016). “Characterization of polyamide powders for determination of laser sintering processability”. In: *European Polymer Journal* 75, pp. 163–174.
- Wang, Chao et al. (2021). “Machine learning for metal additive manufacturing: predicting temperature and melt pool fluid dynamics using physics-informed neural networks”. In: *Materials Today* 50, pp. 361–372.
- Wortberg, Johannes et al. (2012). “Prediction of PA12 melt viscosity in Laser Sintering by a Time and Temperature dependent rheological model”. In: *RTe Journal*.
- Yan, Anru et al. (2022). “The microstructure and cracking behaviors of pure molybdenum fabricated by selective laser melting”. In: *Materials* 15.18, p. 6230.
- Yang, Yabin et al. (2020). “A comprehensive thermal-fluid model for selective laser melting with In Situ experiment verification”. In: *Additive Manufacturing* 32, p. 101082.
- Yue, Pengtao (2020). “Thermodynamically consistent phase-field modelling of contact angle hysteresis”. In: *Journal of Fluid Mechanics* 899, A15. doi: [10.1017/jfm.2020.465](https://doi.org/10.1017/jfm.2020.465).
- Zeng, Zhi et al. (2019). “Improvement on selective laser sintering and post-processing of polystyrene”. In: *Polymers* 11.6, p. 956.